

1     **Thrusts control the thermal maturity of accreted sediments.**

2     Utsav Mannu<sup>1,5\*</sup>, David Fernández-Blanco<sup>2</sup>, Ayumu Miyakawa<sup>3</sup>, Taras Gerya<sup>4</sup>, and Masataka Kinoshita<sup>5</sup>

3     <sup>1</sup>Discipline of Earth Sciences, Indian Institute of Technology, Gandhinagar 382355, India;

4     <sup>2</sup>Barcelona Center for Subsurface Imaging, Passeig Marítim de Barceloneta 37-49, Barcelona Spain

5     <sup>3</sup> Geological Survey of Japan, AIST, Central 7, Higashi 1-1-1, Tsukuba, Ibaraki, 305-8567, Japan

6     <sup>4</sup>Institute of Geophysics, Department of Earth Sciences, ETH Zurich, Sonneggstrasse, 5, 8092 Zurich, Switzerland

7     <sup>5</sup>Earthquake Research Institute, The University of Tokyo, 1-1-1 Yayoi Bunkyo-ku, Tokyo, 113-0032, Japan

8     \**Correspondence to:* Utsav Mannu ([utsav.mannu@iitgn.ac.in](mailto:utsav.mannu@iitgn.ac.in))

9

10

11

12

13

14

15

16

17

18

19

20 **Abstract.**

21 Thermal maturity assessments of hydrocarbon-generation potential and thermal history rarely consider how upper-  
22 plate structures developing during subduction influence the trajectories of accreted sediments. Our  
23 thermomechanical models of subduction support that thrusts evolving under variable sedimentation rates and  
24 décollement strengths fundamentally influence the trajectory, temperature, and thermal maturity of accreting  
25 sediments. This is notably true for the frontal thrust, which pervasively partitions sediments along a low and a high  
26 maturity path. Our findings imply that interpretations of the distribution of thermal maturity cannot be detached  
27 from accounts of the length and frequency of thrusts and their controlling factors. Our approach takes these factors  
28 into consideration and provides a robust uncertainty estimate in maximum exposure temperatures as a function of  
29 vitrinite reflectance and burial depth. As a result, our models reduce former inconsistencies between predicted and  
30 factual thermal maturity distributions in accretionary wedges.

31

32

33

34

35

36

37

38

39

40

41

42

## 44 **1. Introduction**

45 Organic material transforms into coal, oil, and gas at rates primarily controlled by temperature. This transformation,  
46 critical for the hydrocarbon industry, is also useful to study the tectonic and sedimentary evolution of basins and  
47 orogens. The extent of this transformation in sediments, known as thermal maturity, can be measured as vitrinite  
48 reflectance, i.e., the percentage of incident light reflected from the surface of vitrinite particles in those sediments.  
49 Thermal maturity has been used to estimate the thermal evolution of igneous intrusions and seismic slip, the extent  
50 of low-grade metamorphism, porosity, and compaction in basin sediments, and the geothermal history of accreting  
51 material during subduction (e.g., Bostick and Pawlewicz, 1984; Rabinowitz et al., 2020; Fukuchi et al., 2017;  
52 Kamiya et al. 2017).

53 Inferences on the geothermal history of subduction margins based on thermal maturity depend on the  
54 trajectory followed by the accreting sediments (Miyakawa et al., 2019). Low-temperature, high-pressure  
55 metamorphic rocks in the subduction wedge are often attributed to the pressure maxima that typically predate the  
56 temperature maxima in accreted sediments undergoing diagenesis in the wedge (van Gool and Cawood, 1994).  
57 However, the existence of complicated patterns in sediment trajectories is supported by numerical models and field  
58 observations (Giunchi & Ricard, 1999). As the orogenic wedge evolves, sediments accreting along different paths  
59 reach different depths and velocities and are exposed to different regional peak temperatures. Miyakawa et al.  
60 (2019) proposed to subdivide these trajectories based on their final characteristics, like thermal maturity. In this  
61 manner, the spatiotemporal evolution of sediments and their thermal maturity is regulated to a first order by the  
62 partition of incoming sediments along two endmember pathways; (I) a deeper path leading to elevated thermal  
63 maturities and constituted by underthrust material, the *high thermal-maturity path*, and (II) a shallower path that

64 typically lies closer to the surface or gets frequently exhumed to near-surface levels, the *low thermal-maturity*  
65 *path*.

66 Previous studies have used numerical and analogue approaches to study the trajectories of sedimentary  
67 particles, and their spatial and pressure-temperature evolution, as a function of changes in erosion, sedimentation,  
68 or décollement strength. The trajectory followed by underthrust sedimentary units is primarily determined by  
69 orogenic wedge dynamics and its controlling forces (Plat, 1986). Although these sediments may only be exhumed  
70 near the backstop of the wedge, the trajectories of other accreted sediments generally deflect toward the surface  
71 under the influence of erosion (Konstantinovskaia and Malavieille, 2005). In fact, sedimentary particle trajectories  
72 gradually shift from deflection toward the surface near the front of accretion to final exhumation near the wedge  
73 backstop (Wenk and Huhn, 2013). Still, even under-thrust sediments, which would co-relate to high-maturity  
74 paths in our study, have variable pressure-temperature paths (Ruh, 2020). It is important to highlight that the  
75 majority of past studies have explored a snapshot of sediment trajectories, assuming that the general nature of  
76 trajectories remains relatively fixed with time or is stationary in nature. However, the intrinsic connection between  
77 thermal maturity and the comprehensive thermal exposure along the entire trajectory necessitates an in-depth  
78 investigation into the dynamic and transitory nature of sediment trajectories.

79 Although there is general consensus on the rate and extent of sediment trajectory transition from horizontal  
80 to vertical during accretion, the dynamic perturbations in sediment dynamics have yet to be adequately examined.  
81 For instance, while most studies show a great degree of correlation between the initial depth of incoming sediments  
82 and their final position in the wedge (e.g., Mulugeta and Koyi, 1992; Willett, 1992), a dynamic fluctuation in this  
83 correlation due to thrusting can result in non-stationary exhumation paths for accreting sediments in a wedge (e.g.,  
84 Konstantinovskaia and Malavieille, 2005; Miyakawa et al., 2019). Much remains to be explored regarding the  
85 partition of high and low thermal maturity paths and how sediments travel inside natural wedges, given the

86 conventional assumption that accreting sediments remain at the same relative depth and translate along the adjacent  
87 “layers” without vertical mixing throughout the tectonic evolution of the wedge (Hori and Sakaguchi, 2011).

88 Our assessment identifies a primary gap in existing research: the prediction and mapping of the initial  
89 sediment influx to their location in the orogenic wedge. More specifically, the challenge lies in determining which  
90 portions of incoming sediment will predominantly constitute the core of the wedge and which will reside at  
91 comparatively shallower depths. Given that the maximum exposure temperature estimation from the thermal  
92 maturity is inherently reliant on the path of sediments inside the wedge, information on path diversity would  
93 inherently constrain the uncertainty in maximum exposure temperature used for the identification of paleothermal  
94 structures of subduction zones. Moreover, to better understand the time-depth paths of wedge sediments, their  
95 dependence on the initial state of undeformed sediments, and thus their thermal maturity, the factors that control  
96 the evolution of subduction-accretion systems, like sedimentation, erosion, and décollement strength, ought to be  
97 considered (Mannu et al., 2016; Simpson, 2010).

98 Here, we explore in detail the impact of accretion in a subduction wedge has on the thermal maturity of its  
99 sediments. We simulate subduction-accretion using 2D finite-difference thermomechanical models incorporating  
100 empirical thermal conductivity values from the Nankai accretionary margin. We track the evolution of thermal  
101 maturity by computing vitrinite reflectance ( $\%R_o$ ) on each marker and throughout the model, using three well-  
102 established methods of  $\%R_o$  computation, as accretion develops the wedge under different sedimentation rates and  
103 décollement strengths. These factors notably alter the trajectories and thermal maturities of incoming sediments.  
104 Particularly, thrusts define sharp thermal maturity boundaries leading to stark differences in the thermal maturity  
105 of sediments that accrete in different thrust blocks, even when they follow similar trajectories and lay nearby.

106 **2. Geological settings and model generalization**

107 We use a generalized model for the subduction of an oceanic plate under a continental plate, with explicit  
108 integration of key parameters from the Nankai subduction margin off the Kii island in southwest Japan. The Nankai  
109 subduction margin is a product of the ongoing, northwest-directed subduction of the Philippine Sea Plate beneath  
110 the Amurian Plate at a convergence rate of 4.1-6.5 cm/yr (Seno et al., 1993; Miyazaki and Heki, 2001; DeMets et  
111 al., 2010). Past studies posit the initiation of this subduction within the Nankai region at circa 6 Ma (Kimura et al.,  
112 2014). The accretionary wedge adjacent to the Nankai margin is marked by the accretion of thick sediment layers  
113 (>1 km), predominantly formed by overlying younger trench sediments atop Shikoku Basin sediments. Mean  
114 sedimentation rates of ~0.4 mm/yr for this area are calculated from sediment data onland and may largely reach the  
115 trench through submarine channels (Korup et al., 2014).

116 Another reason to select the Nankai subduction margin is that it is a particularly well-studied accretionary margin  
117 regarding its paleo-thermal history and thermal maturity distribution. For example, Underwood et al. (1993) and  
118 Sakaguchi (1999) used thermal maturity estimates from Shimanto accretionary wedge in the Nankai subduction  
119 margin to suggest that ridge subduction can explain the resulting paleo-heat flow. Following this, Ohmori (1997)  
120 published a distribution of thermal maturity and maximum exposure temperature for the Shimanto accretionary  
121 wedge identifying out-of-sequence thrusting in the region. The accretionary wedge adjacent to the Kumano forearc  
122 basin in the Nankai subduction margin has also been the subject of the NanTroSEIZE (Nankai Trough Seismogenic  
123 Zone) project, which drilled C0002 borehole during the 2012 Integrated Ocean Discovery Program Expedition 338.  
124 C0002 borehole is located approximately km southwest of Japan's Kii Peninsula in the Kumano Basin, within the  
125 Nankai accretionary margin, and extends 3,348 meters below the seafloor. Having data on both thermal maturity  
126 and thermal conductivity from the same borehole in subduction wedges is quite uncommon. To our knowledge, the  
127 C0002 borehole, located next to the Kumano forearc basin, is the only place where such data can be found in an

128 accretionary wedge. Because of this unique characteristic, the C0002 borehole serves as an excellent dataset for  
129 validation purposes. We modify the thermal conductivity computation for sediments and décollement (see Table  
130 1) to match the empirical relationship between depth and thermal conductivity, as measured on core samples in the  
131 borehole C0002 (Sugihara et al., 2014).

132 While these adjustments render our models somewhat specific to the Nankai accretionary wedge, we propose that  
133 the thermal conductivity values and trend are representative of patterns typically observed in forearc basins and  
134 accretionary wedges across the globe, making it broadly applicable to general subduction margins. For instance, in  
135 our simulations, the sediment thermal conductivity within our wedge steadily increases with depth from 0.96-4.0  
136  $\text{Wm}^{-1}\text{K}^{-1}$ , which is within the range of thermal conductivity estimates for comparable depth in other subduction  
137 zones, such as the Hikurangi subduction margin, Japan Trench, and Taiwan subduction zone (Fig. S1, Henrys et  
138 al. 2003, Lin et al. 2014, Chi and Reed, 2008). As a result, we compare our simulation results not only to thermal  
139 maturity values in the Nankai accretionary margin but also to those of the Miura-Boso plate subduction margin in  
140 central Japan and the fold and thrust belts of the Western Foothills complex in western Taiwan.

### 141 **3. Methods**

142 We employ I2VIS, a conservative finite-difference 2-D thermomechanical subduction-accretion model with visco-  
143 plastic/brittle rheology (Gerya and Yuen, 2003a, 2003b). The code solves the governing equations for the  
144 conservation of mass, momentum, and heat as well as the advection equation with a non-diffusive marker-in-cell  
145 scheme constrained by thermal conductivity values inferred from Nankai accretionary wedge. Our numerical  
146 approach has several advantages over earlier attempts to simulate thermal maturity in an accretionary wedge, such  
147 as a more realistic geothermal profile, variable particle paths, and thermal evolution. In the following sections, we  
148 provide information regarding the governing equations, the modified thermal conductivity formulations based on

149 the C0002 borehole, boundary conditions, the rheological model, model setup, surface processes, and the  
150 computation of thermal maturity.

### 151 **3.1 Governing equations**

152 The mass conservation is described by the continuity equation with the Boussinesq approximation of  
153 incompressibility.

$$154 \quad \frac{\partial v_x}{\partial x} + \frac{\partial v_y}{\partial y} = 0 \quad (eq. 1)$$

155 Where  $v_x$  and  $v_y$  are horizontal and vertical components of velocity.

156 The equation for conservation of momentum with an incompressibility assumption is expressed in the 2D- Stokes  
157 equation, for the  $x$ -axis and  $y$ -axis, respectively,

$$158 \quad \frac{\partial \sigma_{xx}}{\partial x} + \frac{\partial \sigma_{xy}}{\partial y} = \frac{\partial P}{\partial x} \quad (eq. 2)$$

159 where  $\sigma_{xx}$ ,  $\sigma_{xy}$ ,  $\sigma_{yy}$  are components of the deviatoric stress tensor;  $x$  and  $y$  denote the horizontal and vertical  
160 coordinates and  $P$  is pressure.

$$161 \quad \frac{\partial \sigma_{yy}}{\partial y} + \frac{\partial \sigma_{xy}}{\partial x} = \frac{\partial P}{\partial y} - g\rho(T, P, C) \quad (eq. 3)$$

162 where  $\rho$  is rock density and depends on rock type( $C$ ), temperature( $T$ ), and pressure as  $\rho(T, P) = \rho_0(1 -$   
163  $\xi(T - T_0))(1 + \zeta(P - P_0))$  where  $\xi$  is the coefficient of thermal expansion taken to be  $3 \times 10^{-5} \text{ K}^{-1}$  for all rock  
164 markers and 0 for air/water,  $\zeta$  is the coefficient of compressibility is taken to be  $1 \times 10^{-5} \text{ MPa}^{-1}$  for all rock markers



165 and 0 for air/water,  $\rho_0$  is the reference density at reference temperature ( $T_0 = 298.15 K$ ) and reference pressure  
166 ( $P_0 = 10^5 K$ ).

167 The thermal equation used in the model is as follows:

$$168 \quad \rho C_p \frac{DT}{Dt} = \frac{\partial q_x}{\partial x} + \frac{\partial q_y}{\partial y} + H_r + H_a + H_s \quad (eq.4)$$

169 where,

$$170 \quad q_x = -k(T, C, y) \frac{\partial T}{\partial x}, \quad q_y = -k(T, C, y) \frac{\partial T}{\partial y} \quad (eq.5)$$

$$171 \quad H_a = T \xi \frac{DP}{Dt}, \quad H_s = \sigma_{xx} \dot{\epsilon}_{xx} + \sigma_{yy} \dot{\epsilon}_{yy} + \sigma_{xy} \dot{\epsilon}_{xy} + \sigma_{yx} \dot{\epsilon}_{yx}, \quad H_r = const \quad (eq.6)$$

172 Where  $\frac{D}{Dt}$  is the Lagrangian time derivative, and, respectively;  $\dot{\epsilon}_{xx}$ ,  $\dot{\epsilon}_{xy}$ ,  $\dot{\epsilon}_{yy}$  are components of the strain rate  
173 tensor;  $q_x, q_y$  are the components of heat flux in the horizontal and vertical direction;  $g$  is the vertical gravitational  
174 acceleration;  $C_p$  is the isobaric heat capacity;  $H_r, H_a, H_s$  denote the radioactive, adiabatic and shear heat production,  
175 respectively.  $k(T, C, y)$  is the thermal conductivity, a function of composition, depth, and temperature (Table 1).  
176 The radioactive heat production  $H_r$  is constant for a rock type as mentioned in Table 1.

177 In order to accurately assess thermal maturity, it is crucial to consider the temperature distribution, which  
178 necessitates a realistic thermal conductivity profile when modeling thermal maturity. Many geodynamic models  
179 assume that thermal conductivity decreases as temperature increases, following a defined relationship (e.g., Clauser  
180 and Huenges, 1995). These models typically predict a decrease in thermal conductivity with depth within  
181 accretionary wedges, as geothermal profiles tend to increase in temperature with depth. However, empirical data

182 reveal a different trend: thermal conductivity increases with depth, primarily due to sediment porosity influencing  
 183 shallow thermal conductivity (Henry et al. 2003, Lin et al. 2014). Additionally, the thermal conductivity values  
 184 calculated using the Clauser and Huenges model (1995) are significantly higher than those observed at shallow  
 185 depths (< 3 km). To address these disparities, we incorporate the observed empirical relationship between depth  
 186 and thermal conductivity from the IODP Site C0002 borehole in the Nankai accretionary wedge into our  
 187 simulations. By adjusting the thermal conductivity formulation for sediments based on temperature and depth, we  
 188 aim to replicate the empirical relationship observed in the core samples taken from the borehole at IODP Site C0002  
 189 (Sugihara et al., 2014) and account for the decrease in thermal conductivity near the surface caused by increased  
 190 porosity. We modify the thermal conductivity formulation for sediments as a function of temperature and depth as  
 191 follows.

$$192 \quad k_{sed} = k_0 + \frac{807}{T + 77} \left( 1 - \exp\left(\frac{-Z^2}{1.3e^7}\right) \right) \quad (eq. 6)$$

193  $k_0 = 0.96$  and  $1.5$  for the wedge sediment and décollement respectively. The larger thermal conductivity of the  
 194 décollement emulates higher heat transfer in shear zones due to fluid advection (Fig. S1).

### 195 **3.2 Rheological model**

196 The expression for effective creep viscosities ( $\eta_{eff}$ ) is computed as follows.

$$197 \quad \eta_{disl} = 0.5(\epsilon_{II})^{\frac{1}{n}-1} A_D^{\frac{1}{n}} \exp\left(-\frac{E_a + V_a P}{nRT}\right) \quad (eq. 7)$$

$$198 \quad \eta_{diff} = 0.5 \frac{A_D}{S^{n-1}} \exp\left(-\frac{E_a + V_a P}{RT}\right) \quad (eq. 8)$$

199 
$$\eta_{eff} = \left( \frac{1}{\eta_{disl}} + \frac{1}{\eta_{diff}} \right)^{-1} \quad (eq. 9)$$

200 where  $R$  is the gas constant (8.314 J/K/mol), and,  $A_D, n, m, E_a$  and  $V_a$  are experimentally determined rheological  
 201 parameters:  $A_D$  is the material constant ( $\text{Pa}^{-n}\text{s}^{-1}\text{m}^{-m}$ ),  $n$  is the stress exponent,  $m$  is the grain size exponent,  $E_a$  is  
 202 activation energy (J/mol),  $V_a$  is activation volume (J/Pa), and  $S$  is a stress factor for diffusion creep assumed to be  
 203  $3 \times 10^4 \text{ Pa}$ .

204 
$$\varepsilon_{II} = \sqrt{\frac{\dot{\varepsilon}_{ij} \cdot \dot{\varepsilon}_{ij}}{2}} \quad (eq. 10)$$

205 The model uses visco-plastic rheology to account for both brittle rheology of the shallower and colder rigid  
 206 lithosphere and deeper, hotter ductile lithosphere and asthenosphere. Using the plastic yield threshold as per the  
 207 Drucker-Prager criterion we limit effective viscosity as

208 
$$\eta_{eff} \leq \frac{P \cdot \sin\varphi \cdot (1 - \lambda) + C \cdot \cos\varphi}{2\varepsilon_{II}} \quad (eq. 11)$$

209 where  $C$  is cohesion and  $\varphi$  is an effective internal angle of friction or  $\mu = \tan \varphi$  where is the coefficient of internal  
 210 friction and  $\lambda$  the fluid pressure ratio assumed to be 0 in all the simulations.

### 211 **3.3 Boundary conditions**

212 A free-slip boundary condition is implemented on all boundaries, except on the lower boundary, which is permeable  
 213 in the vertical direction. On the lower boundary we implement an external free slip condition similar to where a  
 214 free slip condition is satisfied at an external boundary such that

215 
$$\frac{\partial V_x}{\partial x} = 0, \text{ and } \frac{\partial V_y}{\partial y} = \frac{V_y}{\Delta Y_{external}} \quad (\text{eq. 10})$$

216 Where,  $V_x$  and  $V_y$ , are the velocities in the horizontal and vertical directions at the boundary,  $\Delta Y_{external}$  is the depth  
 217 that lies outside the modeling domain, and where free slip condition is maintained. Similarly, we set thermally  
 218 insulating boundary conditions on all sides except the lower one where the external thermal boundary condition is  
 219 implemented.

220 **3.4. Surface processes**

221 The rock-water/air boundary is simulated by an adaptive irregular grid that is advected horizontally and vertically  
 222 and is coupled to the thermomechanical grid which controls the tectonic deformation of the surface. Apart from the  
 223 tectonic changes, surface processes prescribed in the model can also change the topography. The surface process  
 224 in the model is controlled by the conversion of rock markers to air/water and vice versa. All sedimentation in the  
 225 model happens as a focused deposition of sediments from sea to land in morphological depressions (e.g., trench)  
 226 is modelled as follows (Fig. S2)

227 
$$y_{new} = y_{old} + K \cdot y_{fill} \quad (\text{eq. 11})$$

228 where  $K = \min \left( \frac{V_{budget}}{V_{basin}}, 1 \right)$

229 The shape of the basin and the resolution of the surface grid can lead to overfilling or underfilling when using the  
 230 equation mentioned above to fill the basin. To address this issue, we calculate the volume of deposited sediments  
 231 and adjust for any deficit or overfill in the subsequent step. This ensures that, over time, the total amount of  
 232 sedimentation remains consistent with the prescribed value. However, it is challenging to ensure that all sediments  
 233 added in a particular step are accommodated within the basins, especially in models with high sedimentation rates

234 where significant runoff occurs. Therefore, the sedimentation rates mentioned in this study are computed as  
235 effective sedimentation rates after the model runs, rather than being predetermined. We perform multiple models  
236 runs (approximately 100) with sedimentation rates uniformly distributed in the range of 0.1-0.9 mm/yr. From these  
237 runs, we select models that exhibit appropriate sedimentation rates. This selection process ensures that the average  
238 sedimentation rates across all our models (ranging from 0.1-0.9 mm/yr) fall within the observed sedimentation rates  
239 in our chosen natural equivalent, the Nankai accretionary wedge in the southwestern subduction margin of Japan  
240 (Korup et al., 2014). For more specific information about the model run and prescribed sedimentary conditions,  
241 please refer to Table 2

### 242 **3.5 Thermal maturity calculation**

243 The model computes the %R<sub>o</sub> of each marker to estimate the thermal maturity of sediments during the model run  
244 using three widely used methods of thermal maturity modelling Easy%R<sub>o</sub> (Burnham and Sweeney, 1989, Sweeney  
245 and Burnham 1990), Simple%R<sub>o</sub> (Suzuki et al., 1993) and Basin%R<sub>o</sub> (Nielsen et al., 2017). All the models  
246 presented here employ a simplified parallel Arrhenius reaction model, which accommodates an array of activation  
247 energies for every component of the kerogen, allowing it to estimate thermal maturity under varying temporal and  
248 thermal scales. The Easy%R<sub>o</sub> model by Sweeney and Burnham (1990) can be described using the following  
249 equations:

$$250 \quad x_i(t) = x_{0i} \exp\left(-\int A \exp\left(-\frac{E_{ai}}{RT(t)}\right) dt\right) \quad (\text{eq. 12})$$

$$251 \quad X(t) = \sum_{i=1}^N x_i(t) \quad \text{eq. 13}$$

$$252 \quad F(t) = X(t = 0) - X(t) \quad (\text{eq. 14})$$

253 
$$\%R_o = \%R_{o0} \exp(3.7F) \quad (eq. 15)$$

254 where,  $x_{oi}$  are weights of reactions for  $i^{\text{th}}$  component of the kerogen also described as the stoichiometric coefficient,  
255  $A$  is the pre-exponential factor,  $E_{ai}$  is the activation energy of the  $i^{\text{th}}$  component of the kerogen,  $R$  is the gas constant,  
256  $T(t)$  is the temperature history,  $F$  is the amount of fixed carbon as a percentage and  $\%R_{o0}$  is the vitrinite reflectance  
257 of the immature unaltered sediment. Sweeney and Burnham (1990) provided a set of 20 activation energies ( $E_{ai}$ )  
258 and the stoichiometric coefficient ( $x_{oi}$ ) listed in Table 3. All thermal models used in this study use the same method  
259 of vitrinite reflectance computation albeit with different sets of activation energies, stoichiometric coefficient, pre-  
260 exponential factor and  $\%R_{o0}$ . Table 3 provides a comprehensive list of all these parameters.

261 All these approaches for computing  $\%R_o$  yield similar trends albeit with different absolute values. In the interest of  
262 clarity, we have mostly illustrated Easy $\%R_o$ , which is the most extensively used method for Vitrinite Reflectance  
263 computation and hereafter we refer Easy $\%R_o$  as  $\%R_o$ , unless explicitly stated.  $\%R_o$  is set to  $\%R_{o0}$  in sediment  
264 markers at the start of the model till 2.5 Myr, while  $\%R_o$  in markers for other rocks, air, and water is undefined at  
265 all times. After 2.5 Myr, the model computes  $\%R_o$  on each marker as a function of temperature ( $T$ ), time ( $t$ ), and  
266 amount of fixed carbon as a percentage ( $F$ ). The initial  $\%R_o$  of newly deposited sediments is computed using an  
267 assumed water-sediment interaction temperature assumed to be the same as the thermocline. The thermocline used  
268 in the model has been estimated using the data obtained and made freely available by International Argo Program  
269 and the national programs that contribute to it for the region near Nankai (Fig. S3; <https://argo.ucsd.edu>,  
270 <https://www.ocean-ops.org>).

### 271 **3.5 Model setup**

272 The modelling domain is 3500 km wide and 350 km deep and is divided into  $3484 \times 401$  nodes populated with  
273  $\sim 125$  million markers (Fig. 1). The high resolution of 220 m (horizontal)  $\times$  130 m (vertical) that we assign at the

274 site of accretionary wedge evolution, decreases steadily toward the edges of the modelling domain to a minimum  
275 resolution of 3000 m x 3200 m. The simulation consists of an oceanic plate converging with a velocity of ~5 cm/yr  
276 and subducting beneath a continental plate (Fig. 1). The convergence is prescribed internally using highly viscous  
277 nodes inside the oceanic and continental plates near the boundary of the models. The oceanic plate consists of a 1-  
278 km-thick upper oceanic crust and a 7-km-thick lower crust (Akuhara, 2018). The thickness of the oceanic lithosphere  
279 depends on its age which is set to 20 Myr at the start of the simulation (Turcotte and Schubert, 2002). The initial  
280 age of the oceanic lithosphere corresponds to the age of the subducting lithosphere in the Nankai subduction margin  
281 (Zhao et al. 2021). Displacement along the megathrust, at the contact between subducting oceanic plate and the  
282 overriding continental plate, occurs in a relatively weak basal layer in accretionary wedges across the globe (Byrne  
283 and Fisher, 1990). We simulate this with a predefined configuration at the interplate, with a 350-meter-thick weak  
284 décollement below a sediment layer that is a km thick. The wedge forms above this interphase by the accretion of  
285 sediments against the continental plate. The continental plate consists of an upper and lower continental crust with  
286 thicknesses of ~20 km and ~15 km, respectively (Akuhara, 2018), and is underlain by a mantle lithosphere of ~25  
287 km. We use a thin (10 km) "sticky air" layer to overlay the top face of the rock strata inside the model which is a  
288 fluid with a low viscosity of  $5 \times 10^{17}$  Pa·s, and a low density, similar to air (white in Fig. 1) or water (light blue in  
289 Fig. 1) (Crameri et al., 2012). The transition between the lithosphere and asthenosphere is prescribed to occur at  
290 1300°C. A weak layer is emplaced at the junction of both plates, which fails mechanically and leads to subduction  
291 initiation. All sediments (light and dark brown in Fig. 1) are rheologically identical, but colours are alternated in  
292 time to allow tracking the development of different geological structures. Readers are referred to Table 1 for the  
293 rheological and thermal properties of all the materials used. Note that in our models, we refer to the measure all  
294 distances from the point where the continental and oceanic plates initially and is situated 1850 km from the right  
295 boundary of the modelling area. The terms "landward" and "seaward" indicate the relative direction towards the  
296 continental plate or the oceanic plate, respectively. The "Backstop" refers to the edge of the continental plate that

297 buttresses the wedge and acts akin to an indenter for the accretionary wedge. The "forearc high" represents the  
298 highest point in the forearc zone, which includes both the accretionary wedge and the forearc basin.

299

### 300 ***3.6 Experimental Strategy***

301 Here, we present a total of 10 simulations that vary in their effective basal friction or their effective sedimentation  
302 rate to discern patterns of thermal maturity evolution in wedge sediments. Models  $M_0^{4.5} - M_0^{14.5}$  have no  
303 sedimentation and effective internal angle values for the décollement of  $\varphi_b = 4.5^\circ, 7^\circ, 9.5^\circ, 12^\circ$  and  $14.5^\circ$   
304 respectively. The chosen range of effective décollement strength is well within the range of values postulated by  
305 several studies for the Nankai accretionary wedge (Tesei et al., 2015). The rest of the models ( $M_{0.1}^{9.5} - M_{0.9}^{9.5}$ ) and  
306 have a medium-strength décollement and variable effective sedimentation rate ranging from 0.1 to 0.9 mm/yr. In  
307 all the models presented in this study, sedimentation is limited to the trench, extending from the sea to the land.  
308 Restricting sedimentation to the trench allows us to observe and analyze the length and frequency of thrust sheets,  
309 enabling comprehensive investigation of their role in determining sediment trajectories. With these models, we  
310 evaluate the particle trajectory and %R<sub>o</sub> of accreting sediments as a function of décollement strength and  
311 sedimentation rate. To restrict the number of parameters influencing our observations, models have no erosion.  
312 Moreover, all models lack surface processes during the first ~2.5 Myr and have sedimentation thereafter. Strain-  
313 softening has been modeled as a linear decrease of angle of friction ( $\varphi$ ) and cohesion between cumulative strain of  
314 0.5 and 1.5. Sediments used in the model have an angle of friction ( $\varphi$ ) of  $30^\circ$  before a cumulative strain of 0.5 and  
315 a strain-softened value of  $20^\circ$  after a threshold of 1.5 cumulative strain. Strain softening has been used in wedges  
316 to mimic the weakening of faults and shear zones due to lubrication with values threshold taken from previous  
317 numerical studies (Hickman et al., 1995 , Ruh et. al. 2014 ).



#### 318 4. Results

319 In our models, subduction begins at 0.1 Myr by failure of the weak material between continental and oceanic plate  
320 (Fig. 2, Fig. S4-S13 , also [see supporting information movies](#)). Continued and sustained accretion of sediments  
321 against the deforming continental crust forms the accretionary wedge from the interplate contact landwards. After  
322  $\sim 5$  Myr, all models develop a distinct wedge in agreement with the critical wedge theory (Davis et al., 1983).  
323 Surface slopes, measured by fitting a line in the surface of the wedge for every timestep between 2.5-7.5 Myr and  
324 reported as mean  $\pm$  standard deviation, increase systematically, as effective basal friction increases from  $\sim 4.5^\circ$  to  
325  $\sim 14.5^\circ$  (Fig. 1, Fig S4-S13, Table 2,  $M_0^{4.5} - M_0^{14.5}$ ). Whereas models with a relatively weaker décollement, as  
326 ( $M_0^{4.5}, \varphi_b = 4.5^\circ$ ), have surface slopes of  $0.95^\circ \pm 0.3^\circ$ , models with very strong décollement, as ( $M_0^{14.5}, \varphi_b = 14.5^\circ$ ),  
327 have slopes as steep as  $5.9 \pm 1^\circ$  (Table 2). Our estimations of surface slopes consistently exhibit an excess of  
328 approximately  $1.5^\circ$  compared to the surface slopes predicted by the critical wedge theory (Table 2). This is probably  
329 due to the penetration of weaker decollement material into high shear zones, resulting in faults that are weaker than  
330 the strain-softened wedge material.

331

332 Models without trench sedimentation grow solely by accretion of incoming seafloor sediments, with frequent  
333 nucleation of frontal thrusts. Models with weaker décollements develop thrust sheets that are lengthier but remain  
334 active for shorter periods. This is clear when comparing, for models with increasingly strong décollement  
335 ( $M_0^{4.5}, M_0^7, M_0^{9.5}, M_0^5, M_0^{14.5}$ ), the average distance between first and second frontal thrusts are  $15.5 \pm 7.0$  km,  $12.1$   
336  $\pm 3.6$  km,  $8.8 \pm 3.3$  km,  $8.7 \pm 2.1$  km and  $8.0 \pm 1.8$  km, respectively. Increasing sedimentation rate also leads to an  
337 increase in thrust sheet length from  $7.3 \pm 1.1$  km for model  $M_{0.1}^{9.5}$  to  $13.8 \pm 7.8$  km in model  $M_{0.9}^{9.5}$ .

338

339 In models with similar basal friction, models with higher sedimentation rates have lengthier thrust sheets that  
340 remain active for longer periods (Table 2). Steeper surface slopes with increased décollement strengths and change

341 in thrust sheet length with sedimentation and décollement strength are well-known effects that have been  
342 confirmed by previous numerical (Ruh et al., 2012) and analogue (Malavieille and Trullenque, 2009; Storti and  
343 McClay, 1995) models. All the reported values are mean  $\pm$  Standard Deviation values recorded between 2.5-7.5  
344 Myr in individual models. All models exhibit a temperature gradient that corresponds well with the temperature  
345 profile observed in the boreholes at IODP Site C0002 in the Kumano forearc basin, on top of the Nankai  
346 accretionary wedge (Fig. S14).

347

#### 348 ***4.1 Thermal maturity of the wedge***

349 Sediments are more thermally mature in wedges that have a higher sedimentation rate or décollement strength. For  
350 example, the mean %R<sub>o</sub> of simulations for wedges with the highest sedimentation is 12% higher (0.75) than in  
351 those without sedimentation ( $M_0^{4-5}$ , Table 2, Fig. 3). Similarly, simulations of wedges with the strongest  
352 décollement have the highest mean %R<sub>o</sub> (0.94) of all the simulations presented in this study.

353 Thermal maturity values increase with depth and landward distance from the trench to the forearc high  
354 irrespective of the decollement strength, sedimentation rates and method of thermal maturity computation (Fig. 3-  
355 4). The absolute value of %R<sub>o</sub> and the rate at which thermal maturity values increase landward from the trench are  
356 larger for wedges with high décollement strength (Fig. 4A). For wedges characterized by the same décollement  
357 strength but higher trench sedimentation, we observe that the rate of thermal maturity increases in a landward  
358 direction from the trench and remains consistent across these wedges (Fig. 4B). Comparing the values of %R<sub>o</sub>  
359 along a horizontal marker at the depth of trench in several models emphasizes this result; the model with the highest  
360 décollement strength reaches a maximum %R<sub>o</sub> of 1.25 and has the highest rate of landward increase in thermal  
361 maturity (Fig. 4A). However, all models with similar décollement strength but different sedimentation do not  
362 visibly vary in their rate or magnitude of landward increase in thermal maturity. All models show a decrease in

363 thermal maturity landward of the forearc high, commonly of 0.2 %R<sub>o</sub>. Other interesting observations that we  
364 explore below are the increased thermal maturity occurring in the vicinity of thrusts and the reversal in sediment  
365 maturity around out-of-sequence thrust active over longer times visible across several models (e.g. Fig. 3).

366 The magnitude of %R<sub>o</sub> varies consistently among Easy%R<sub>o</sub>, Simple%R<sub>o</sub> and Basin%R<sub>o</sub>. On average  
367 Easy%R<sub>o</sub> have the smallest values, followed very closely by Basin%R<sub>o</sub> (with an average difference of only 0.02).  
368 However, Simple%R<sub>o</sub> had the highest average value of thermal maturity, being 0.16 and 0.13 higher than Easy%R<sub>o</sub>  
369 and Basin%R<sub>o</sub> (Fig. 3).

#### 370 *4.2 Sediment trajectory inside the wedge*

371 In wedges with a higher décollement strength or sedimentation rate, sediments tend to follow high-maturity paths  
372 in larger proportions. We demonstrate this effect by creating a map of the thermal maturity of sediments at 7.5 Myr  
373 of the model run, mapped to their spatial position at 2.5 My of the model run to analyse the spatial correlation  
374 between sediment position (depth and distance) from the trench and thermal maturity (Fig. 5). We also show the  
375 mean thermal maturity attained by sediments at a given horizontal distance from the trench during this period by a  
376 dashed black line in Fig. 5. The scatter plot shows sharp changes in eventual thermal maturity with horizontal  
377 distance from the trench that relate to changes in sediment trajectory. The mean thermal maturity is also variable  
378 along the horizontal length of the wedge and has a periodicity ( $\Lambda$ ) increasing in distance with higher sedimentation  
379 rate but relatively constant with changing basal friction (Fig. 5). The periodicity of mean %R<sub>o</sub> was computed by  
380 finding the average wavelength of the auto-correlated mean %R<sub>o</sub>. Whereas the mean thermal maturity has a short  
381 periodicity of ~7.2 km for the model  $M_0^{9.5}$  with no sedimentation rates, the model  $M_0^{9.5}$  shows the longest periodicity  
382 of 21 km. However, for all models with no sedimentation ( $M_0^{4.5} - M_0^{14.5}$ ), the periodicity remains relatively  
383 consistent between the range of 7-8 km.

384 Fig. 3 also represents the distribution of trajectories that exist in an accretionary wedge and how these  
385 trajectories get impacted under trench sedimentation (a subset of these trajectories can be viewed in the  
386 supplementary Fig. S15). Whereas in wedges with weak décollements ( $M_0^{4.5}$ ), none of the shallowest half of  
387 incoming sediments reach  $\%R_o > 1$  in 5 Myr, 2% of sediments reach this value in wedges with strong décollement  
388 ( $M_0^{14.5}$ ). The effects of décollement strength in the thermal maturity of sediments can be quantified as well at deeper  
389 levels, with one-eighth vs more than half of the sediments surpassing values of  $\%R_o = 1$  for the deepest half of  
390 incoming sediments (12% and 54% respectively) in weak vs strong-decollement wedges ( $M_0^{4.5}$  vs  $M_0^{14.5}$ ),  
391 respectively. In wedges for the model without sedimentation ( $M_0^{9.5}$ ), the top half of the incoming sediments  
392 fail to achieve  $\%R_o > 1$ , as opposed to  $\sim 15\%$  of them reaching  $\%R_o > 1$  in the models with a sedimentation rate  
393 of 0.9 mm/yr ( $M_0^{9.5}$ ). In sum, the proportion of sediments in the top half and bottom half of the wedge that reach  
394 high maturity steadily increases with both sedimentation rate and décollement strength (Table 2).

### 395 ***4.3 Patterns of trajectory and thermal maturity in incoming sediments***

396 The diversity in the trajectory of sediments in the wedge leads to a plethora of pathways in which the sediments  
397 can become thermally mature and thus introduces epistemic uncertainty in the estimation of maximum exposure  
398 temperature. Fig. 6, captures this uncertainty where we plot the maximum exposure temperature as a function of  
399  $\%R_o$  for all the models simulated in this study. The colours in for individual markers represent the depth of the  
400 markers normalized by the thickness of the wedge represented as  $Y_n$  (See Fig S16 for mode details). We find that  
401 almost all the models show a remarkable similarity in their relationship between maximum exposure temperature  
402 and  $\%R_o$  (for individual models please see Fig. S16) and differ mostly in their proportion of sediments with extreme  
403 values of  $\%R_o$ . We observe that the typical uncertainty in maximum exposure temperature increases with an  
404 increase in values of  $\%R_o$  with  $\sim 15^\circ\text{C}$  interval at around  $\%R_o=0.2$  compared to  $\sim 33^\circ\text{C}$  interval at  $\%R_o= 3$  (both for

405 95% confidence interval, Fig. 6b). Moreover, we observe that incorporating information about the normalized depth  
406 of sediments ( $Y_n$ ) significantly aids in constraining the maximum exposure temperature. For instance, although the  
407 overall uncertainty at  $\%R_o=1$ , is  $\sim 23^\circ\text{C}$ , for sediments with a  $Y_n$  of 0.2-0.4, the uncertainty greatly reduces to only  
408  $\sim 10.5^\circ\text{C}$ . Thus, the range of thermal maturity values for sediments clearly has a large correlation with their  
409 trajectories.

#### 410 ***4.4 Comparison of Easy% $R_o$ , Simple% $R_o$ , and Basin% $R_o$***

411 The usage of Easy% $R_o$ , Simple% $R_o$ , and Basin% $R_o$  in our models provides us with a distinct perspective on the  
412 comparative (dis)advantages of each method in estimating thermal maturity values. The non-uniqueness of  
413 maximum exposure temperatures for the same values of  $\%R_o$  arises from the variation in sediment trajectory and  
414 thermal exposure. This diversity among sediment markers results in multiple markers attaining the same level of  
415 thermal maturity. We refer to the range of maximum exposure temperatures corresponding to similar  $\%R_o$  values  
416 as the uncertainty in maximum exposure temperatures. Uncertainty for all three models increases with increasing  
417  $\%R_o$  from  $\sim 20\text{--}25^\circ\text{C}$  at  $\sim 0.3$  to  $\sim 35^\circ\text{C}$  at  $\%R_o=3.5$  (Fig. 6b). Easy% $R_o$ , probably the best-recognised method of  
418 thermal maturity computation, yields the best constraint on uncertainty for very small changes nearing  $<1$  values.  
419 For the values of  $\%R_o$  between 1 and 3, all models yield very similar uncertainty, with Simple% $R_o$  yielding the  
420 most constrained exposure temperatures (Fig. 6b). However, beyond  $\%R_o=3$ , Simple% $R_o$  becomes unreliable, with  
421 uncertainty in exposure temperatures as high as  $55^\circ\text{C}$  at  $\%R_o=4$ . Easy% $R_o$  yields an uncertainty range of  $\sim 37^\circ\text{C}$   
422 till  $\%R_o=4.4$ , and starts to be unreliable above this value. Basin% $R_o$  remains consistent until a very high value of  
423  $\%R_o \sim 6$ , and thus provides the best constraint on the widest range of values of thermal maturity (Fig. 6b).

## 424 **5. Discussion**

425 The thermomechanical models presented in this study provide (a) an explanation for the trend in thermal maturity  
426 observed in accretionary wedges, (b) a new venue to explore the uncertainty in the estimation of maximum exposure  
427 temperature using vitrinite reflectance, and (c) an estimate of the minimum lateral distance between the trench and  
428 the location of a paleo-thermal anomaly on the subduction plate for it to be identified after accretion.

429

### 430 *5.1 Thermal maturity distribution and importance of thrusting in wedges*

431 Collectively, our results support a general increase of thermal maturity with depth and landward in accretionary  
432 wedges. The thermal maturity increase with depth is primarily the result of progressively larger exposures to higher  
433 temperatures as depth of burial increases. On the contrary, the landward increase in thermal maturity is caused by  
434 the long-term deformation of sediments accumulated at older times and the exhumation of sediments that were  
435 underthrust as they meet the backstop. Our models demonstrate that the rate of landward thermal maturity  
436 increase is faster for thicker wedges, both for the case of sediment near the surface and deep inside the wedge (Fig.  
437 4). This can be attributed to a larger proportion of sediments being exposed to higher temperatures over an extended  
438 duration within thicker wedges, but validating this result with natural observations remains challenging, given to  
439 the very limited availability of thermal maturity data across natural wedges. Accretionary wedges in our models  
440 can be simplified as a system where the subducting oceanic plate acts as the primary heat source, while the seafloor  
441 acts as a heat sink. The heat generated through other sources such as shear heating, radioactivity, and advection is  
442 relatively insignificant compared to the heat originating from the younger oceanic plate. In our simulations, we  
443 consider a relatively younger and hotter oceanic plate of approximately 20 Myr, which is consistent with the  
444 accretionary wedge in the Nankai region adjacent to the Kumano forearc basin (Zhao et al., 2021). Given that the  
445 convergence rate remains constant across all models, the heat received from the oceanic plate should remain  
446 relatively similar. However, as the wedge thickness increases, the temperature gradient between the boundaries of

447 the wedge must become gentler, resulting in a larger portion of the wedge experiencing elevated temperatures.  
448 Moreover, frequent advection from the subduction channel also results in elevated temperatures in the core of the  
449 wedge. Finally, models with thicker wedges typically exhibit higher décollement strength, leading to increased  
450 shear heating at the base of the wedge. Observational studies conducted by Yamano et al. (1992) on the thermal  
451 structure of the Nankai accretionary prism have further highlighted that the landward increase in prism thickness  
452 is the most significant factor contributing to temperature variations within the wedge. Consequently, the sustained  
453 higher temperatures within thicker wedges over time would lead to a higher rate of landward thermal maturity.

454 Our models show two cases where the above-mentioned trend in thermal maturity is relevantly altered, which we  
455 nominate "on-fault increase" and "fault-block inversion". For instance, Fig. 3 shows a steep rise in the thermal  
456 maturity of sediments at fault sites. Thermal maturity inversions by thrusting, which are commonplace in  
457 accretionary contexts, are the primary cause of thermal maturity differentiation among wedges with similar paleo-  
458 thermal structures. During fault-block inversions, the positive gradient of thermal maturity with depth is inverted  
459 as relatively mature sediments are thrust over less mature sediments (Underwood et al., 1992). The strong  
460 differentiation in the trajectory of sediments led by thrusting has a larger influence over thermal maturity than their  
461 burial depth or their in-wedge location. This novel inference has probably remained concealed thus far due to the  
462 large number of parameters that condition thrust development, frequency, length, and thermal state and the lack of  
463 high-resolution thermal maturity data.

464 The thermal maturity that incoming sediments reach also varies periodically as a function of thrust frequency. By  
465 examining the lateral and vertical position of incoming sediments and their eventual thermal maturity, we can  
466 deduce that the overall movement of sediments in the wedge is predominantly layered but not stationary over time.  
467 Changes in the depth of the thermal maturity boundary are less frequent and have larger amplitudes with increased  
468 décollement strength, and especially, increased sedimentation rates (Fig. 5). The periodicity in the thermal maturity

469 boundary marks the periodic oscillation of the predominant trajectory followed by incoming sediments, i.e. between  
470 accretion (low thermal maturity path) and under-thrusting (high-thermal maturity path). As a result, it should also  
471 strongly correlate with the periodicity observed in the evolution of forearc topography (Menant et al., 2020) and  
472 the frequency of thrust formation in our models. This is expected, given that thrusts are active over longer mean  
473 times, and they channel material toward the décollement more efficiently, in wedges with stronger décollement or  
474 increased sedimentation. While sediments at internal and higher structural positions of the wedge are translated  
475 toward the surface and have a lower thermal maturity, sediments at external and lower structural positions are  
476 translated toward the décollement and have a relatively higher maturity. The entire cycle is repeated with the  
477 formation of new in-sequence thrust.

478 This is a relevant observation for it typifies the causality of particular sediment grains following a high or low  
479 maturity path, a long-standing unanswered question (Miyakawa et al., 2019). We corroborate this observation by  
480 analyzing the terminal thermal maturity of sediments across a frontal thrust active at a younger age. An example in  
481 Fig. 7 shows the thermal maturity of sediments at  $\sim 7.5$  Myr across a thrust active at  $\sim 4$  Myr. Whereas this occurs  
482 for all thrusts in the wedge, the frontal thrust is particularly pronounced in partitioning sediments into the high and  
483 low maturity paths. Thermal maturity correlates with sediment depth weakly near faults and more strongly away  
484 from them. The distance of sediment from the frontal thrust dictates the trajectory of sediment grains, and as a  
485 result, the pressure-temperature conditions to which they are exposed.

486 Our results show the need to consider all factors influencing fault frequency when inferring the geothermal history  
487 of contractional terrains by means of thermal maturity. In this study, we have considered solely how décollement  
488 strength and the rate of trench sedimentation vary the frequency, architecture, and overall behavior of thrusts, and  
489 the frontal thrust, as the wedge evolves. Fortunately, this predictive exercise should be relatively straightforward,  
490 for the impact of these external factors on the fault structure of wedges has been established (Fillon et al., 2012;



491 Mannu et al., 2016, 2017; Mugnier et al., 1997; Simpson, 2010; Storti and McClay, 1995), and the effect of each of  
492 these factors can be accounted for when assessing the trajectory of sediments and the distribution of thermal  
493 maturity in accretionary wedges. It is nevertheless important to note that the frequency of faults in a wedge can be  
494 impacted by many other factors, including hinterland sedimentation (Storti and McClay, 1995; Simpson, 2010;  
495 Fernández-Blanco et al. 2020), erosion (Konstantinovskaia, 2005; Willett, 1992), and seafloor topography  
496 (Dominguez et al., 2000).

## 497 ***5.2. Implications of thermal maturity evolution in a subduction wedge***

498 The main implications of this contribution emerge from its predictive power. Our approach can predict to a precise  
499 degree the thermal maturity of sediments and the uncertainty associated with the maximum exposure temperature  
500 in accretionary contexts with known structuration. A more accurate quantification of the thermal evolution and  
501 thermal state of accreted sediments reduces the uncertainties attached to the location of temperature-led  
502 transformations of organic material into hydrocarbons in subduction margins and other accretionary contexts. Such  
503 increased accuracy in the distribution of thermally mature sediments may also be applied for improved assessments  
504 of the evolution in time of any other geothermal process, including seismic slip, magmatic and metamorphic extent,  
505 porosity, compaction, and diagenesis of sediments, and the reconstruction of convergent margins in general  
506 (Bostick and Pawlewicz, 1984; Mählmann and Le Bayon, 2016; Rabinowitz et al., 2020; Sakaguchi et al., 2011;  
507 Totten and Blatt, 1993; Underwood et al., 1992).

508 Our simulations also imply that the paleo-thermal information stored in the incoming sediments can only be  
509 retrieved if sediments are at appropriate locations with respect to emergent thrusts. We illustrate this using two runs  
510 of the same model and tracking an artificial thermal anomaly imposed on incoming sediments at two different  
511 locations (Fig. 8). This hypothetical thermal anomaly can be conceptualized as any alteration of the thermal

512 maturity profile of incoming sediments, for example, elevated heat flows by an antecedent magmatic intrusion.  
513 While the change in %Ro associated with the short-lived thermal anomaly results in abnormally high values of  
514 thermal maturity in both sediment packages, it can only be retrieved for the end-model run of sediments located  
515 further from the trench (those in the right panel, Fig. 8B). Contrarily, the end-model run of sediments closer to the  
516 trench (those in the left panel, Fig. 8A) shows no signs of discontinuity in the thermal maturity distribution of the  
517 wedge. This is because we deliberately placed the thermal anomaly at sites that evolve at two structural locations  
518 during the model run, i.e., above and below a yet-undeveloped frontal thrust (Fig. 8). The sediment sector affected  
519 by the thermal anomaly closer to the trench is overthrust by the frontal thrust and remains in a footwall location  
520 thereafter (Fig. 8a). In contrast, the homologous sedimentary package further away from the trench is accreted by  
521 the frontal thrust and remains in a hanging-wall location (Fig. 8b). Thus, the preservation of the record of an  
522 antecedent thermal anomaly is only possible in the former case. We further note that, in our simulations, the entire  
523 vertical column of sediments records the thermal anomaly, while in nature, the anomaly may affect only sediments  
524 at the deeper locations of the sedimentary pile, which are in turn the sediments that most likely to follow a high-  
525 maturity path. We thus regard the possibility of retrieving such antecedent geothermal information as minimal.

526 Finally, among the three methods of %Ro computation, Easy%Ro and Basin%Ro are more consistent and well-  
527 constrained on a wide range of thermal maturities in comparison to Simple%Ro, which seems to be particularly  
528 useful for a smaller range of thermal maturity values. This simply illustrates the fact that while Easy%Ro and  
529 Basin%Ro computation deals with several parallel reactions related to the maturity of kerogen (and hence multiple  
530 activation energies), Simple%Ro is based on best-fitted single activation energy, and hence yields large confidence  
531 intervals at the extreme %Ro values. Additionally, the inclusion of the higher activation energy reactions in  
532 Basin%Ro makes it the best-suited formulation for sediments at the deeper and shear zone sediments which usually  
533 get saturated using Easy%Ro.

### 534 *5.3 Comparisons to previous numerical studies*

535 The thermomechanical models presented in this study offer a dynamic representation of trajectories within the  
536 wedge. Although the averaged trends in thermal structure and sediment trajectories remain consistent, there are  
537 short-term dynamic fluctuations near the frontal thrust. These fluctuations contribute to a diverse range of sediment  
538 paths along the depth of the incoming sediments. Miyakawa et al. (2019) conducted a similar study, modeling  
539 vitrinite reflectance using Simple% $R_o$  and a stationary thermal field, which also resulted in an increase in thermal  
540 maturity towards the continent and thermal maturity inversions due to thrusting. However, the use of Simple% $R_o$   
541 led to premature saturation and the disappearance of thermal maturity variations at a shallower depth in their model.

542 We can compare our findings with other geodynamic models that examine the thermal structure of the wedge,  
543 although there are only a limited number of numerical models of thermal maturity in wedges. Pajang et al. (2022)  
544 recently investigated the distribution of the brittle-ductile transition in wedges and proposed a region dominated by  
545 viscous shear near the backstop, with the wedge core reaching temperatures of 450°C and typically containing  
546 forearc basins. Although trench sedimentation in our model does not result in the formation of forearc basins, the  
547 overall flattening of the wedge slope and the high vitrinite reflectance in the core align with consistent structures.  
548 Moreover, the presence of highly mature sediments in the wedge core suggests compacted sediments with greater  
549 strength and higher P-wave velocity. Although empirical studies have shown a strong correlation between  $V_p$  and  
550 thermal maturity estimates for depths of up to 4 km (Baig et al, 2016, Mallick et al. 1995), the exact nature of this  
551 correlation may vary depending on the specific location. Nevertheless, the patterns of thermal maturity values in  
552 the wedge core in our models also correspond to the patterns of P-wave velocity observed in the Nankai and  
553 Hikurangi margins (Górszczyk et al., 2019; Nakanishi et al., 2018; Dewing and Sanei, 2009; Arai et al., 2020).

554 Two modes of sediment trajectory evolution, from incoming sediment to their position inside the wedge, are  
555 generally considered; depth dependence sediment trajectories, as observed in studies by Mulugeta and Koyi, (1992)  
556 and Hori and Sakaguchi (2011), and crossover exhumation pathways, as illustrated by Konstantinovskaia et al.  
557 (2005) and Miyakawa (2019). We consider the latter as non-stationary sediment trajectories that vary with time  
558 and cut across sediment trajectories of sediments previously located at the same spatial position. Our models show  
559 that both modes of sediment trajectories are valid, and that changes in trajectory patterns leading to path crossovers  
560 are controlled by the horizontal distance of sediments from the frontal thrust. Starting at a threshold distance from  
561 the trench, sediments at different depths follow laminar paths along different trajectories within the wedge.  
562 Laminar-type trajectories can be reproduced in a broad range of simulations and are particularly common in models  
563 with low sedimentation and décollement strengths. However, the depth dependence of sedimentary paths varies  
564 periodically as a function of distance from the trench of specific sedimentary packages (Fig. 5). This effect, which  
565 is particularly marked in the neighbourhood of the frontal thrust, explains the crossover paths for incoming  
566 sedimentary packages at similar depths but different horizontal locations (Konstantinovskaia et al. 2005).  
567 Therefore, thrust faults in the wedge act as the primary agent controlling whether sediments sustain depth-  
568 controlled laminar flow or sediment mixing.

#### 569 ***5.4 Comparisons to natural wedges***

570 Our models achieve thermal maturity distributions that are in good agreement with their natural analogues, despite  
571 several relevant assumptions. Our models are very simplified with regard to their natural analogues, with  
572 assumptions such as no elasticity, predefined décollement, no erosion, and simple and uniform rheology. Also, our  
573 models have an insufficient resolution for small-scale fault activity and lack empirical relations to simulate the  
574 compaction of sediments and multiscale fluid flow. Although these assumptions hinder a wholesale comparison  
575 between our simulations and natural examples of accretionary wedges, we still find an acceptable agreement

576 between our model and natural observations, primarily due to simulations that have a temperature evolution  
577 assimilating empirical data and a fine spatiotemporal resolution. Our estimated %R<sub>o</sub> values for the model are in  
578 very good agreement with those measured for the borehole C0002 Nankai accretionary wedge by Fukuchi et al.  
579 2009 (Fig. 9). The maximum exposure temperature estimated from the observed thermal maturity for the C0002  
580 borehole also strongly correlates with maximum temperatures recorded on markers in the model with similar  
581 thermal maturity with 95% confidence (Fig. S17). However, our result is reliant on the empirical thermal  
582 conductivity profiles estimated for the C0002 borehole, which does not show any large thermal discontinuity  
583 between the forearc basin and inner wedge that has been observed in fossil accretionary wedges (e.g., Underwood  
584 et al. 1989).

585 Landward increase in thermal maturity is well documented in studies of the Japan trench, at the Miura–Boso plate  
586 subduction margin, the fold and thrust belts Western Foothills complex in western Taiwan, the Mesozoic  
587 accretionary prism in the Franciscan subduction complex in northern California, as well as Cretaceous Shimanto  
588 accretionary complex in Nankai subduction margin (Yamamoto et al. 2017; Sakaguchi et al. 2007; Underwood et  
589 al, 1989; Sakaguchi, 1999). The natural wedges mentioned above display vitrinite reflectance values with  
590 maximum %R<sub>o</sub> values ranging from 0.2 to 4.0 near the surface, which is generally much higher than the near-  
591 surface %R<sub>o</sub> values observed in our models. Underwood et al. (1989) suggested that this discrepancy is likely due  
592 to the ongoing process of progressive exhumation and erosion, leading to the exposure of deeper sections of the  
593 accretionary prism over time. As a result, younger wedges, such as those found in the Miura–Boso plate subduction  
594 margin, exhibit a much closer resemblance to the %R<sub>o</sub> values near the surface of our our models.

595 On-fault increases in vitrinite reflectance are well also documented in nature, as for boreholes C0004 and C0007,  
596 which sample the megasplay fault in Nankai accretionary margin (Sakaguchi et al., 2011). The vitrinite reflectance  
597 data from the megasplay and frontal thrusts in Nankai indicate the faults reach a temperature well in excess of  
598 300°C during an earthquake, much larger than the background thermal field. Therefore, on-fault increases in

599 thermal maturity are comparatively smaller in our simulations and lack the marked increase in %Ro observed at  
600 fault sites in nature. We consider this is due to a discrepancy in the rate of change of thermal diffusion occurring  
601 in simulated thrusts, given that our models develop much wider fault zones than their natural equivalents. For  
602 instance, the location of megasplay fault in C0007 borehole exhibits an unevenness within the high-reflectance  
603 zone with a maximum %R<sub>o</sub> ~1.9 (Sakaguchi et al., 2011). This is in line with the prediction by Fulton and Harris  
604 (2012) about the impact of fault thickness on change in vitrinite reflectance. Natural observations also exhibit a  
605 much higher incidence of on-fault increase in thermal maturity compared to our simulations, given that our models  
606 do not have sufficient spatial resolution to capture the large number of thin faults that develop inside the wedge.  
607 Natural examples of fault-block inversion have been well-documented in natural settings, providing evidence of  
608 past thrust activity preserved in the shallower sections of the Nankai accretionary wedge. Sakaguchi (1999) reported  
609 the presence of step increments of thermal maturity, similar to increments in vitrinite reflectance in Fig. 3 and 4  
610 across the faults. Other examples are the fault block inversion along the Fukase Fault in the Shimanto accretionary  
611 wedge (Ohmori et al., 1997) and the inversion beneath the forearc basin in the Nankai accretionary wedge (Fukuchi  
612 et al., 2017).

613 Our study highlights that paleo-thermal anomalies that extend laterally beyond the average thrust spacing have a  
614 significantly higher likelihood of being retained in the final thermal maturity record of the wedge. This allows  
615 several inferences. For example, the subduction of the Cretaceous ridge, as identified by Underwood et al. (1993)  
616 and Sakaguchi (1999), must have caused a substantial alteration in thermal maturity during the Kula-Pacific  
617 subduction in order to be discernible in vitrinite reflectance records. Likewise, we can anticipate the preservation  
618 of the paleo-thermal anomaly near Ashizuri in the southern Nankai wedge, which has high thrust frequency, in  
619 contrast to that at the Muroto transect, where thrust sheets are widely spaced. In the case of the accretionary wedge  
620 adjacent to the Boso peninsula, Kamiya et al. (2017) proposed the emplacement of an ophiolite complex beneath  
621 the Miura group. Our findings indicate that the preservation of the thermal-advection heating event coincided with

622 a decrease in trench sedimentation. This likely led to an increase in the thrust frequency, which facilitated the  
623 preservation of the thermal-advection heating event in the thermal maturity data.

## 624 **6. Conclusion**

625 This study demonstrates how contractional faults alter the paths of sediments as they accrete and how this  
626 fundamentally controls the distribution of the thermal maturity of sediments in accretionary wedges and emphasizes  
627 the role that sedimentation rate and interplate contact strength have in such distribution. The increased resolution  
628 of our approach leads to findings that have relevant implications. For example, the geothermal history that can be  
629 retrieved from the thermal maturity of sediments in drills, i.e., at the shallow wedge, provides, at best, an incomplete  
630 record that is skewed towards the thermal evolution of sediments near the trench. Coevally, relevant sectors of  
631 sediments located further seaward, when not subducted, follow high-maturity paths that overprint their antecedent  
632 thermal history. Finally, this study also provides a first-order uncertainty measure for the thermal maturity of  
633 sediments based on the diversity in their trajectory.

## 634 **Code/Data availability**

635 I2VIS, vitrinite reflection computation and visualization codes would be made available by the corresponding  
636 author on request.

## 637 **Author contribution**

638 UM was responsible for the conceptualization of the work, original draft writing, and administration of the paper.  
639 DFB contributed to figure visualization, writing and review of the paper. MK and AM contributed to  
640 conceptualization and review. TG provided the I2VIS code and contributed to the review of the paper.

641

642 **Acknowledgments**

643 The authors want to acknowledge the topic editor Susanne Buiters as well as the reviewers Jonas B. Ruh and David  
644 Hindle for constructive and intriguing reviews and feedback on the original and revised manuscript.

645 **Competing interests**

646 The authors declare that they have no conflict of interest.

647 **References**

- 648 1. Akuhara, T. (2018). Receiver Function Image of the Subducting Philippine Sea Plate. Fluid Distribution Along the  
649 Nankai-Trough Megathrust Fault off the Kii Peninsula: Inferred from Receiver Function Analysis, 43-64.
- 650 2. Arai, R., Kodaira, S., Henrys, S., Bangs, N., Obana, K., Fujie, G., ... & NZ3D Team. (2020). Three-dimensional P  
651 wave velocity structure of the Northern Hikurangi margin from the NZ3D experiment: Evidence for fault-bound  
652 anisotropy. *Journal of Geophysical Research: Solid Earth*, 125(12), e2020JB020433.
- 653 3. Baig, I., Faleide, J. I., Jahren, J., & Mondol, N. H. (2016). Cenozoic exhumation on the southwestern Barents Shelf:  
654 Estimates and uncertainties constrained from compaction and thermal maturity analyses. *Marine and Petroleum  
655 Geology*, 73, 105-130.
- 656 4. Bostick, N. H., & Pawlewicz, M. J. (1984). Paleotemperatures based on vitrinite reflectance of shales and limestone  
657 in igneous dike aureoles in the Upper Cretaceous Pierre shale, Walsenburg, Colorado.
- 658 5. Burnham, A. K., & Sweeney, J. J. (1989). A chemical kinetic model of vitrinite maturation and reflectance. *Geo-  
659 chimica et Cosmochimica Acta*, 53(10), 2649-2657.
- 660 6. Chi, W. C., & Reed, D. L. (2008). Evolution of shallow, crustal thermal structure from subduction to collision: An  
661 example from Taiwan. *Geological Society of America Bulletin*, 120(5-6), 679-690.
- 662 7. Clauser, C., & Huenges, E. (1995). Thermal conductivity of rocks and minerals. *Rock physics and phase relations:  
663 a handbook of physical constants*, 3, 105-126.



- 664 8. Davis, D., Suppe, J., & Dahlen, F. A. (1983). Mechanics of fold-and-thrust belts and accretionary wedges. *Journal*  
665 *of Geophysical Research: Solid Earth*, 88(B2), 1153-1172.
- 666 9. DeMets, C., Gordon, R. G., & Argus, D. F. (2010). Geologically current plate motions. *Geophysical journal inter-*  
667 *national*, 181(1), 1-80.
- 668 10. Dewing, K., & Sanei, H. (2009). Analysis of large thermal maturity datasets: Examples from the Canadian Arctic  
669 Islands. *International Journal of Coal Geology*, 77(3-4), 436-448.
- 670 11. Dominguez, Stephane, Jacques Malavieille, and Serge E. Lallemand. "Deformation of accretionary wedges in re-  
671 sponse to seamount subduction: Insights from sandbox experiments." *Tectonics* 19.1 (2000): 182-196.
- 672 12. Fernández-Blanco, D., Mannu, U., Cassola, T., Bertotti G., & Willett SD (2020). Sedimentation and viscosity con-  
673 trols on forearc high growth. *Basin Research*, <https://doi.org/10.1111/bre.12518>
- 674 13. Fillon, C., & van der Beek, P. (2012). Post-orogenic evolution of the southern Pyrenees: Constraints from inverse  
675 thermo-kinematic modelling of low-temperature thermochronology data. *Basin Research*, 24(4), 418-436.
- 676 14. Fukuchi, M., Nii, T., Ishimaru, N., Minamino, A., Hara, D., Takasaki, I., ... & Tsuda, M. (2009). Valproic acid in-  
677 duces up-or down-regulation of gene expression responsible for the neuronal excitation and inhibition in rat cortical  
678 neurons through its epigenetic actions. *Neuroscience research*, 65(1), 35-43.
- 679 15. Fukuchi, R., Yamaguchi, A., Yamamoto, Y., & Ashi, J. (2017). Paleothermal structure of the Nankai inner acce-  
680 tionary wedge estimated from vitrinite reflectance of cuttings. *Geochemistry, Geophysics, Geosystems*, 18(8), 3185-  
681 3196.
- 682 16. Gerya, T. V., & Yuen, D. A. (2003). Characteristics-based marker-in-cell method with conservative finite-differ-  
683 ences schemes for modeling geological flows with strongly variable transport properties. *Physics of the Earth and*  
684 *Planetary Interiors*, 140(4), 293-318.
- 685 17. Gerya, T. V., & Yuen, D. A. (2003). Rayleigh–Taylor instabilities from hydration and melting propel ‘cold plumes’  
686 at subduction zones. *Earth and Planetary Science Letters*, 212(1-2), 47-62.
- 687 18. Gerya, T. V., & Meilick, F. I. (2011). Geodynamic regimes of subduction under an active margin: effects of rheo-  
688 logical weakening by fluids and melts. *Journal of Metamorphic Geology*, 29(1), 7-31.

- 689 19. Górszczyk, A., Operto, S., Schenini, L., & Yamada, Y. (2019). Crustal-scale depth imaging via joint full-waveform  
690 inversion of ocean-bottom seismometer data and pre-stack depth migration of multichannel seismic data: a case  
691 study from the eastern Nankai Trough. *Solid Earth*, 10(3), 765-784.
- 692 20. Gool, J. A. V., & Cawood, P. A. (1994). Frontal vs. basal accretion and contrasting particle paths in metamorphic  
693 thrust belts. *Geology*, 22(1), 51-54.
- 694 21. Heki, K., Miyazaki, S. I., Takahashi, H., Kasahara, M., Kimata, F., Miura, S., ... & An, K. D. (1999). The Amurian  
695 Plate motion and current plate kinematics in eastern Asia. *Journal of Geophysical Research: Solid Earth*, 104(B12),  
696 29147-29155.
- 697 22. Henrys, S. A., Ellis, S., & Uruski, C. (2003). Conductive heat flow variations from bottom-simulating reflectors on  
698 the Hikurangi margin, New Zealand. *Geophysical Research Letters*, 30(2).
- 699 23. Hickman, S., Sibson, R., & Bruhn, R. (1995). Introduction to special section: Mechanical involvement of fluids in  
700 faulting. *Journal of Geophysical Research: Solid Earth*, 100(B7), 12831-12840.
- 701 24. Hori, T., & Sakaguchi, H. (2011). Mechanism of décollement formation in subduction zones. *Geophysical Journal*  
702 *International*, 187(3), 1089-1100.
- 703 25. Kamiya, N., Yamamoto, Y., Wang, Q., Kurimoto, Y., Zhang, F., & Takemura, T. (2017). Major variations in vit-  
704 rinite reflectance and consolidation characteristics within a post-middle Miocene forearc basin, central Japan: A  
705 geodynamical implication for basin evolution. *Tectonophysics*, 710, 69-80.
- 706 26. Kimura, G., Hashimoto, Y., Kitamura, Y., Yamaguchi, A., & Koge, H. (2014). Middle Miocene swift migration of  
707 the TTT triple junction and rapid crustal growth in southwest Japan: A review. *Tectonics*, 33(7), 1219-1238.
- 708 27. Konstantinovskaia, E., & Malavieille, J. (2005). Erosion and exhumation in accretionary orogens: Experimental and  
709 geological approaches. *Geochemistry, Geophysics, Geosystems*, 6(2).
- 710 28. Konstantinovskaya, E., & Malavieille, J. (2011). Thrust wedges with décollement levels and syntectonic erosion: A  
711 view from analog models. *Tectonophysics*, 502(3-4), 336-350.
- 712 29. Korup, O., Hayakawa, Y., Codilean, A. T., Matsushi, Y., Saito, H., Oguchi, T., & Matsuzaki, H. (2014). Japan's  
713 sediment flux to the Pacific Ocean revisited. *Earth-Science Reviews*, 135, 1-16.

- 714 30. Lin, W., Fulton, P. M., Harris, R. N., Tadaï, O., Matsubayashi, O., Tanikawa, W., & Kinoshita, M. (2014). Thermal  
715 conductivities, thermal diffusivities, and volumetric heat capacities of core samples obtained from the Japan Trench  
716 Fast Drilling Project (JFAST). *Earth, Planets and Space*, 66(1), 1-11.
- 717 31. Maehlmann, R. F., & Le Bayon, R. (2016). Vitrinite and vitrinite like solid bitumen reflectance in thermal maturity  
718 studies: Correlations from diagenesis to incipient metamorphism in different geodynamic settings. *International*  
719 *Journal of Coal Geology*, 157, 52-73.
- 720 32. Malavieille, J., & Trullenque, G. (2009). Consequences of continental subduction on forearc basin and accretionary  
721 wedge deformation in SE Taiwan: Insights from analogue modeling. *Tectonophysics*, 466(3-4), 377-394.
- 722 33. Mallick, R. K., & Raju, S. V. (1995). Thermal maturity evaluation by sonic log and seismic velocity analysis in  
723 parts of Upper Assam Basin, India. *Organic Geochemistry*, 23(10), 871-879.
- 724 34. Mannu, U., Ueda, K., Willett, S. D., Gerya, T. V., & Strasser, M. (2016). Impact of sedimentation on evolution of  
725 accretionary wedges: Insights from high-resolution thermomechanical modeling. *Tectonics*, 35(12), 2828-2846.
- 726 35. Mannu, U., Ueda, K., Willett, S. D., Gerya, T. V., & Strasser, M. (2017). Stratigraphic signatures of forearc basin  
727 formation mechanisms. *Geochemistry, Geophysics, Geosystems*, 18(6), 2388-2410.
- 728 36. Menant, A., Angiboust, S., Gerya, T., Lacassin, R., Simoes, M., & Grandin, R. (2020). Transient stripping of sub-  
729 ducting slabs controls periodic forearc uplift. *Nature communications*, 11(1), 1823.
- 730 37. Miyakawa, A., Kinoshita, M., Hamada, Y., & Otsubo, M. (2019). Thermal maturity structures in an accretionary  
731 wedge by a numerical simulation. *Progress in Earth and Planetary Science*, 6(1), 1-13.
- 732 38. Mugnier, J. L., Baby, P., Colletta, B., Vinour, P., Bale, P., & Leturmy, P. (1997). Thrust geometry controlled by  
733 erosion and sedimentation: A view from analogue models. *Geology*, 25(5), 427-430.
- 734 39. Mulugeta, G., & Koyi, H. (1992). Episodic accretion and strain partitioning in a model sand wedge. *Tectonophysics*,  
735 202(2-4), 319-333.
- 736 40. Nakanishi, A., Takahashi, N., Yamamoto, Y., Takahashi, T., Citak, S. O., Nakamura, T., ... & Kaneda, Y. (2018).  
737 Three-dimensional plate geometry and P-wave velocity models of the subduction zone in SW Japan: Implications  
738 for seismogenesis.

- 739 41. Nielsen, S. B., Clausen, O. R., & McGregor, E. (2017). basin% Ro: A vitrinite reflectance model derived from ba-  
740 sin and laboratory data. *Basin Research*, 29, 515-536.
- 741 42. Ohmori, K., Taira, A., Tokuyama, H., Sakaguchi, A., Okamura, M., & Aihara, A. (1997). Paleothermal structure of  
742 the Shimanto accretionary prism, Shikoku, Japan: Role of an out-of-sequence thrust. *Geology*, 25(4), 327-330.
- 743 43. Pajang, S., Khatib, M. M., Heyhat, M., Cubas, N., Bessiere, E., Letouzey, J., ... & Le Pourhiet, L. (2022). The dis-  
744 tinct morphologic signature of underplating and seamounts in accretionary prisms, insights from thermomechanical  
745 modeling applied to Coastal Iranian Makran. *Tectonophysics*, 845, 229617.
- 746 44. Platt, J. P. (1986). Dynamics of orogenic wedges and the uplift of high-pressure metamorphic rocks. *Geological*  
747 *society of America bulletin*, 97(9), 1037-1053.
- 748 45. Rabinowitz, H. S., Savage, H. M., Polissar, P. J., Rowe, C. D., & Kirkpatrick, J. D. (2020). Earthquake slip surfaces  
749 identified by biomarker thermal maturity within the 2011 Tohoku-Oki earthquake fault zone. *Nature communica-*  
750 *tions*, 11(1), 533.
- 751 46. Ruh, J. B., Kaus, B. J., & Burg, J. P. (2012). Numerical investigation of deformation mechanics in fold-and-thrust  
752 belts: Influence of rheology of single and multiple décollements. *Tectonics*, 31(3).
- 753 47. Ruh, J. B., Gerya, T., & Burg, J. P. (2014). 3D effects of strain vs. velocity weakening on deformation patterns in  
754 accretionary wedges. *Tectonophysics*, 615, 122-141.
- 755 48. Ruh, J. B. (2020). Numerical modeling of tectonic underplating in accretionary wedge systems. *Geosphere*, 16(6),  
756 1385-1407.
- 757 49. Sakaguchi, A. (1999). Thermal maturity in the Shimanto accretionary prism, southwest Japan, with the thermal  
758 change of the subducting slab: fluid inclusion and vitrinite reflectance study. *Earth and Planetary Science Letters*,  
759 173(1-2), 61-74.
- 760 50. Sakaguchi, A., Chester, F., Curewitz, D., Fabbri, O., Goldsby, D., Kimura, G., ... & Yamaguchi, A. (2011). Seismic  
761 slip propagation to the updip end of plate boundary subduction interface faults: Vitrinite reflectance geothermome-  
762 try on Integrated Ocean Drilling Program NanTro SEIZE cores. *Geology*, 39(4), 395-398.

- 763 51. Schumann, K., Behrmann, J. H., Stipp, M., Yamamoto, Y., Kitamura, Y., & Lempp, C. (2014). Geotechnical be-  
764 havior of mudstones from the Shimanto and Boso accretionary complexes, and implications for the Nankai accre-  
765 tionary prism. *Earth, planets and space*, 66, 1-16.
- 766 52. Seno, T., Stein, S., & Gripp, A. E. (1993). A model for the motion of the Philippine Sea plate consistent with  
767 NUVEL-1 and geological data. *Journal of Geophysical Research: Solid Earth*, 98(B10), 17941-17948.
- 768 53. Simpson, Guy DH. "Formation of accretionary prisms influenced by sediment subduction and supplied by sedi-  
769 ments from adjacent continents." *Geology* 38.2 (2010): 131-134.
- 770 54. Storti, F., & McClay, K. (1995). Influence of syntectonic sedimentation on thrust wedges in analogue models. *Geol*
- 771 55. Sugihara, T., Kinoshita, M., Araki, E., Kimura, T., Kyo, M., Namba, Y., ... & Thu, M. K. (2014). Re-evaluation of  
772 temperature at the updip limit of locked portion of Nankai megasplay inferred from IODP Site C0002 temperature  
773 observatory. *Earth, Planets and Space*, 66(1), 1-14.
- 774 56. Suzuki, N., Matsubayashi, H., & Waples, D. W. (1993). A simpler kinetic model of vitrinite reflectance. *AAPG bul-*  
775 *letin*, 77(9), 1502-1508.
- 776 57. Sweeney, J. J., & Burnham, A. K. (1990). Evaluation of a simple model of vitrinite reflectance based on chemical  
777 kinetics. *AAPG bulletin*, 74(10), 1559-1570.
- 778 58. Tesei, T., Cruciani, F., & Barchi, M. R. (2021). Gravity-driven deepwater fold-and-thrust belts as Critical Coulomb  
779 Wedges: Model limitations and the role of friction vs. fluid pressure. *Journal of Structural Geology*, 153, 104451.
- 780 59. Totten, M. W., & Blatt, H. (1993). Alterations in the non-clay-mineral fraction of pelitic rocks across the diagenetic  
781 to low-grade metamorphic transition, Ouachita Mountains, Oklahoma and Arkansas. *Journal of Sedimentary Re-*  
782 *search*, 63(5), 899-908.
- 783 60. Turcotte, D. L., & Schubert, G. (2002). *Geodynamics*. Cambridge university press.
- 784 61. Underwood, M. B., Moore, G. F., Taira, A., Klaus, A., Wilson, M. E., Fergusson, C. L., ... & Steurer, J. (2003).  
785 Sedimentary and tectonic evolution of a trench-slope basin in the Nankai subduction zone of southwest Japan. *Jour-*  
786 *nal of Sedimentary Research*, 73(4), 589-602.

- 787 62. Underwood, M. B., O'Leary, J. D., & Strong, R. H. (1988). Contrasts in thermal maturity within terranes and across  
788 terrane boundaries of the Franciscan Complex, northern California. *The Journal of Geology*, 96(4), 399-415.
- 789 63. Underwood, M. B. (1989). Temporal changes in geothermal gradient, Franciscan subduction complex,  
790 northern California. *Journal of Geophysical Research: Solid Earth*, 94(B3), 3111-3125.
- 791 64. Wenk, L., & Huhn, K. (2013). The influence of an embedded viscoelastic–plastic layer on kinematics and mass  
792 transport pattern within accretionary wedges. *Tectonophysics*, 608, 653-666.
- 793 65. Willett, S. D. (1992). Dynamic and kinematic growth and change of a Coulomb wedge. In *Thrust tectonics* (pp. 19-  
794 31). Dordrecht: Springer Netherlands.
- 795 66. Yamano, M., Foucher, J. P., Kinoshita, M., Fisher, A., Hyndman, R. D., Leg, O. D. P., & Party, S. S. (1992). Heat  
796 flow and fluid flow regime in the western Nankai accretionary prism. *Earth and Planetary Science Letters*, 109(3-  
797 4), 451-462.
- 798 67. Zhao, D., Wang, J., Huang, Z., & Liu, X. (2021). Seismic structure and subduction dynamics of the western Japan  
799 arc. *Tectonophysics*, 802, 228743.

800

801

802

803

804

805

806

Rock Type	Reference Density( $\rho_o$ ) (kg/m <sup>3</sup> ) <sup>a</sup>	Cohesion (MPa) <sup>b</sup>	Angle of friction (°) <sup>c</sup>	Thermal Conductivity (W/ (m K)) <sup>d</sup>	Flow law <sup>e</sup>	E (kJ/mol)	n	$H_r$ ( $\mu W/kg$ )	$A_D$ (Pa <sup>n</sup> s <sup>-1</sup> )	V (J $\mu Pa^{-1}$ mol <sup>-1</sup> )
Water	1000	0	0	20		0	0	0	0	0
Air (Sticky-air)	0	0	0	20		0	0	0	0	0
Décollement	2600	0.001	4.5-14.5	$(1.5+807/(T+77))^*$ $(1-\exp(-Z^2/1.3e7))$	Wet quartzite	154	2.3	1.5	$1.97 \times 10^{17}$	8
Sediments1	2600	1/0.05	30/20*	$(0.96+807/(T+77))^*$ $(1-\exp(-Z^2/1.3e7))$	Wet quartzite	154	2.3	1.5	$1.97 \times 10^{17}$	8
Sediments2	2600	1/0.05 <sup>*b</sup>	30/20*	$(0.96+807/(T+77))^*$ $(1-\exp(-Z^2/1.3e7))$	Wet quartzite	154	2.3	1.5	$1.97 \times 10^{17}$	8
Upper Continental Crust	2700	10	31	$0.64+807/(T+77)$	Wet quartzite	300	2.3	1	$1.97 \times 10^{17}$	12
Lower Continental Crust	2800	10	31	$0.64+807/(T+77)$	Plagioclase An75	300	3.2	1	$4.8 \times 10^{22}$	8
Upper Oceanic Crust	3000	10	31	$1.18+474/(T+77)$	Wet quartzite	300	2.3	0.25	$1.97 \times 10^{17}$	8
Lower Oceanic Crust	3000	10	31	$1.18+474/(T+77)$	Plagioclase An75	300	3.2	0.25	$4.8 \times 10^{22}$	8
Mantle Lithosphere	3300	10	31	$0.73+1293/(T+77)$	Dry olivine	532	3.5	0.022	$3.98 \times 10^{16}$	8
Asthenosphere	3300	10	31	$0.73+1293/(T+77)$	Dry olivine	532	3.5	0.022	$3.98 \times 10^{16}$	8

\*Strain-softened Cohesion/Coefficient of friction.

\*We have assumed the flow law parameters such as  $A_D$ , E, V and n to be the same for dislocation and diffusion creep.

T is Temperature in Kelvin, Z is the depth from the seafloor

The reference temperature for densities have been taken as the average temperature of the rock type.

<sup>a</sup>Reference for Densities: Turcotte & Schubert, 2002; Gerya & Meilick, 2011

<sup>b</sup>Reference cohesion values for sediments Schumann et al. 2014

<sup>c</sup>Reference for angle of frictions Schumann et al. 2014, Ruh et. al 2014, Gerya & Meilick, 2011

<sup>d</sup>Reference for thermal conductivity: Clauser & Huenges. (1995), Sugihara et al., 2014

<sup>e</sup>Reference for flow laws and radiogenic heat production: Ranalli 1995, Gerya & Meilick, 2011

813 **Table 2: Model runs and their specific characteristic observations**

Models	$\varphi_b$	$\varphi / \varphi_{ss}$	$\lambda$	<i>SR</i>	<i>L</i>	$\beta(^{\circ})$	$\alpha(^{\circ})$	$\alpha$ predicted ( $\varphi_{ss}/\varphi$ ) ( $^{\circ}$ )	<i>D</i>	$\langle R_o\% \rangle$	% <i>top-half</i>	% <i>Bottom-half</i>
$M_0^{4.5}$	4.5°	30°/20°	0	None	123.2±15.7	4.2±0.6	0.95±0.3	0.03±0.2/-1.3±0.3	15.5±7.0	0.54	0.0	12.7
$M_0^7$	7°	30°/20°	0	None	97.7±9.9	4.9±0.8	2.6±0.8	0.97±0.2/-0.95±0.3	12.1±3.6	0.60	0.0	22.5
$M_0^{9.5}$	9.5°	30°/20°	0	None	77.8±4.8	5.3±0.8	3.7±0.9	2.1±0.4/-0.32±0.3	8.7±2.1	0.67	0.0	31.3
$M_{0.1}^{9.5}$	9.5°	30°/20°	0	0.1	76.1±5.9	5.0±0.9	2.3±0.7	2.3±0.4/-0.12±0.3	7.3±1.1	0.71	0.1	35.3
$M_{0.3}^{9.5}$	9.5°	30°/20°	0	0.3	79.3±8.2	4.9±0.9	2.0±0.5	2.3±0.4/-0.1±0.3	7.8±2.5	0.69	0.1	32.0
$M_{0.5}^{9.5}$	9.5°	30°/20°	0	0.5	79.9±7.4	4.9±0.8	2.1±0.5	2.3±0.4/-0.1±0.2	9.5±4.0	0.71	2.7	34.4
$M_{0.7}^{9.5}$	9.5°	30°/20°	0	0.7	81.3±10.5	5.0±0.9	2.1±0.5	2.3±0.7/-0.11±0.3	9.9±5.0	0.73	4.2	41.5
$M_{0.9}^{9.5}$	9.5°	30°/20°	0	0.9	82.5±11.0	5.0±0.9	2.3±0.7	2.2±0.4/-0.16±0.3	13.8±7.8	0.75	14.6	51.8
$M_0^{12}$	12°	30°/20°	0	None	71.6±5.0	5.6±1.0	5.1±1.0	3.5±0.6/0.4±0.4	8.8±3.3	0.83	1.2	40.6
$M_0^{14.5}$	14.5°	30°/20°	0	None	62.7±6.0	5.9±1.0	6.7±1.4	5.1±0.8/1.2±0.4	8.0±1.8	0.94	2.0	54.0

$\varphi_b$  is décollement Strength (internal angle of friction).

$\varphi$  Sediment Strength.

$\varphi_{ss}$  Sediment Strength (Strain weakened)/ (internal angle of friction).

*SR* Average Sediment rate (mm/yr).

$\lambda$  is pore-fluid pressure ratio.

*L* Average Length of the wedge (in km) between ~2.5-7.5Myr. Length of the wedge is computed as the distance between trench and backstop(set at 1850 km from the right edge of the modelling domain).

$\beta$  Average basal dip angle  $\beta$  (in degrees) between ~2.5-7.5Myr measure by fitting a line in the basal surface.

$\alpha$  Average surface slope angle  $\alpha$  (in degrees) between ~2.5-7.5Myr measure computing the slope of fitting the best fitted line in the surface.

*D* Average Distance between the first and second frontal thrust between ~2.5-7.5Myr (in km). The frontal thrust is always identified from the trench. The send thrust is identified by the high strain rate and deviation of the weak décollement material from the trend of oceanic plate.

$\alpha$  predicted ( $\varphi_{ss}/\varphi$ ) is the surface slope predicted using critical wedge theory using the  $\beta$  observed in the model and sediment strength (Initial /Strain weakened).

*T* Average time a frontal thrust remains active between ~3.5-7.5Myr.

$\langle R_o\% \rangle$  Average vitrinite reflectance of the wedge between ~3.5-7.5 Myr.

%*top* Proportion of >1 eventual  $R_o\%$  (*vitrinite reflectance at 7.5 Myr*) at shallow half of the incoming sediment at 2.5 Myr.

%*bottom* Proportion of >1 eventual  $R_o\%$  (*vitrinite reflectance at 7.5 Myr*) at deep half of the incoming sediments.

\*Please see Fig. S18 for details on the various measurement done on the wedge.

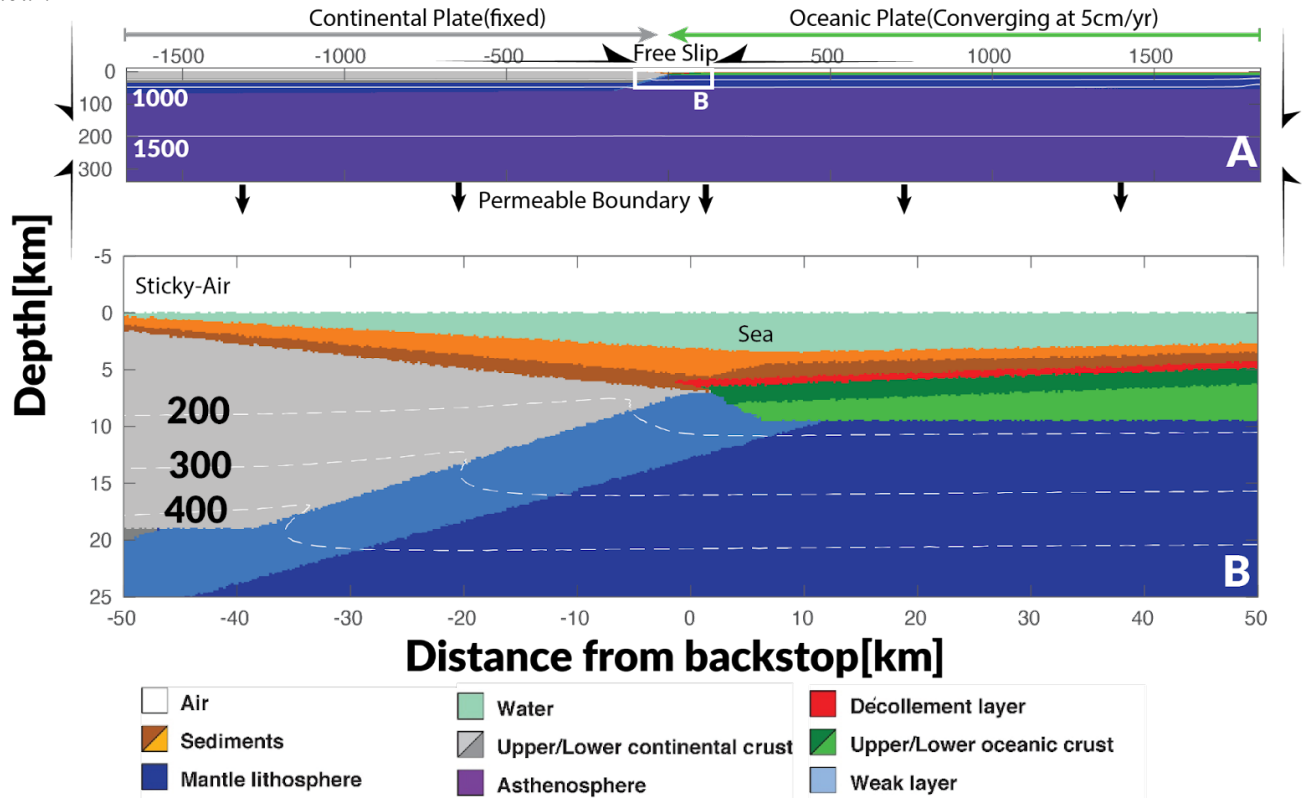


S. No.	Stoichiometric Coefficient for Easy% $R_o$ ( $x_{0i\_Easy}$ )	Activation Energy for Easy% $R_o$ (kJ/mol) ( $E_{ai\_Easy}$ )	Stoichiometric Coefficient for Simple% $R_o$ ( $x_{0i\_Simple}$ )	Activation Energy(E) for Simple% $R_o$ ( $E_{ai\_Simple}$ )	Stoichiometric Coefficient for Simple% $R_o$ ( $x_{0i\_Basin}$ )	Activation Energy(E) for Basin% $R_o$ (kJ/mol) ( $E_{ai\_Simple}$ )
1	0.0300	142256	1	1.38e5	0.0185	142256
2	0.0300	150624	-	-	0.0143	150624
3	0.0400	158992	-	-	0.0569	158992
4	0.0400	167360	-	-	0.0478	167360
5	0.0500	175728	-	-	0.0497	175728
6	0.0500	184096	-	-	0.0344	184096
7	0.0600	192464	-	-	0.0344	192464
8	0.0400	200832	-	-	0.0322	200832
9	0.0400	209200	-	-	0.0282	209200
10	0.0700	217568	-	-	0.0062	217568
11	0.0600	225936	-	-	0.1155	225936
12	0.0600	234304	-	-	0.1041	234304
13	0.0600	242672	-	-	0.1023	242672
14	0.0500	251040	-	-	0.076	251040
15	0.0500	259408	-	-	0.0593	259408
16	0.0400	267776	-	-	0.0512	267776
17	0.0300	276144	-	-	0.0477	276144
18	0.0200	284512	-	-	0.0086	284512
19	0.0200	292880	-	-	0.0246	292880
20	0.0100	301248	-	-	0.0096	301248
$A_{Easy} = 1e13$ and $\%R_{o0} = 0.2$ , $A_{Simple} = 1e13$ and $\%R_{o0} = 0.2$ , $A_{Basin} = 9.7029e12$ and $\%R_{o0} = 0.2104$						

818 **List of Figures**

819 **Fig. 1:**

820 *Initial model setup. A. The lithological and geothermal map of the whole computational domain with boundary conditions. B.*  
 821 *The zoomed lithological and geothermal map of the inset illustrates the junction of continental and oceanic plates. The colors*  
 822 *represent different lithology of the materials used in the models, with upper and lower crust represented by light and dark*  
 823 *grey, upper and lower oceanic crust represented by dark and light green. The arrows around the computational domain*  
 824 *represent the imposed boundary conditions, while the white contour lines (dashed in the zoomed panel) show the geothermal*  
 825 *gradients used for the initial model. The numbers on the white contour lines represent the temperature values in °C for the*  
 826 *contour.*



827 h

828

829

830

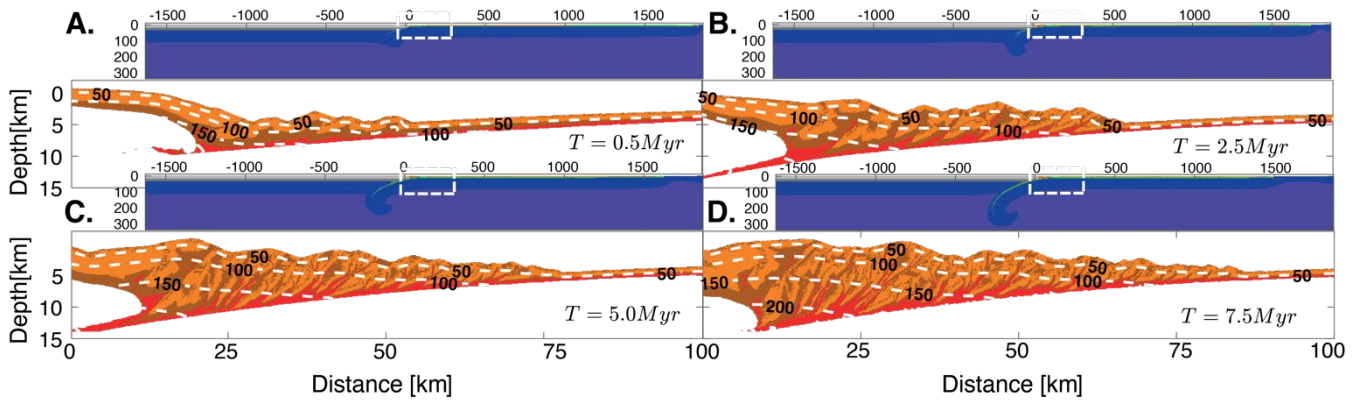
831

832

833

834

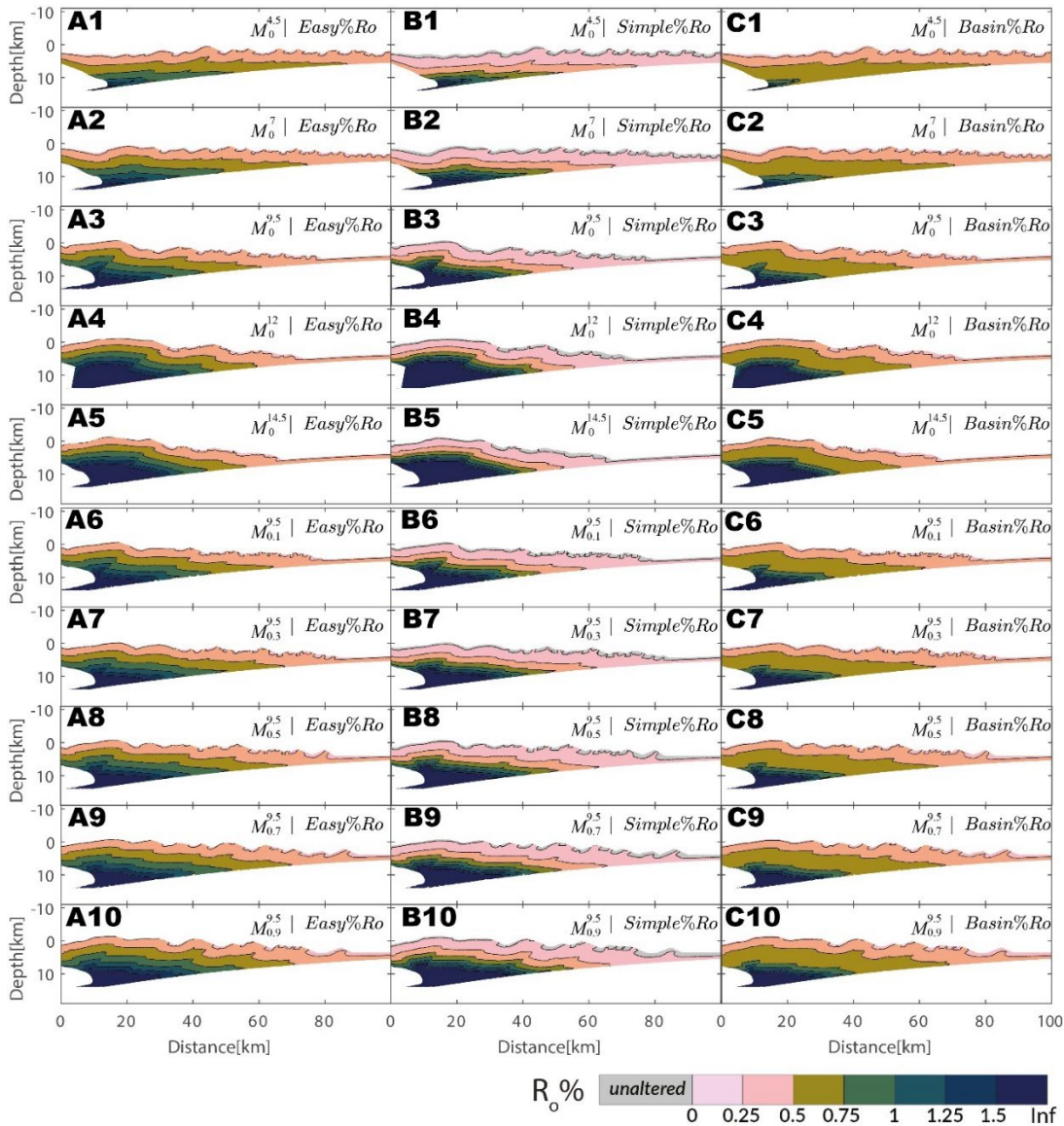
835 **Fig. 2:**  
 836 Typical thermomechanical evolution of the accretionary wedge for model. The illustrated Figure is for the model  $M_0^7$  at (a)0.5  
 837 Myr (b)2.5 Myr (c)5.0 Myr (d) 7.5 Myr. Similar Figures for other models have been illustrated in supplementary images. The  
 838 colormap for the panels is same as Figure 1.  
 839



840  
 841  
 842  
 843  
 844  
 845  
 846  
 847  
 848  
 849  
 850  
 851  
 852  
 853  
 854  
 855  
 856  
 857  
 858  
 859

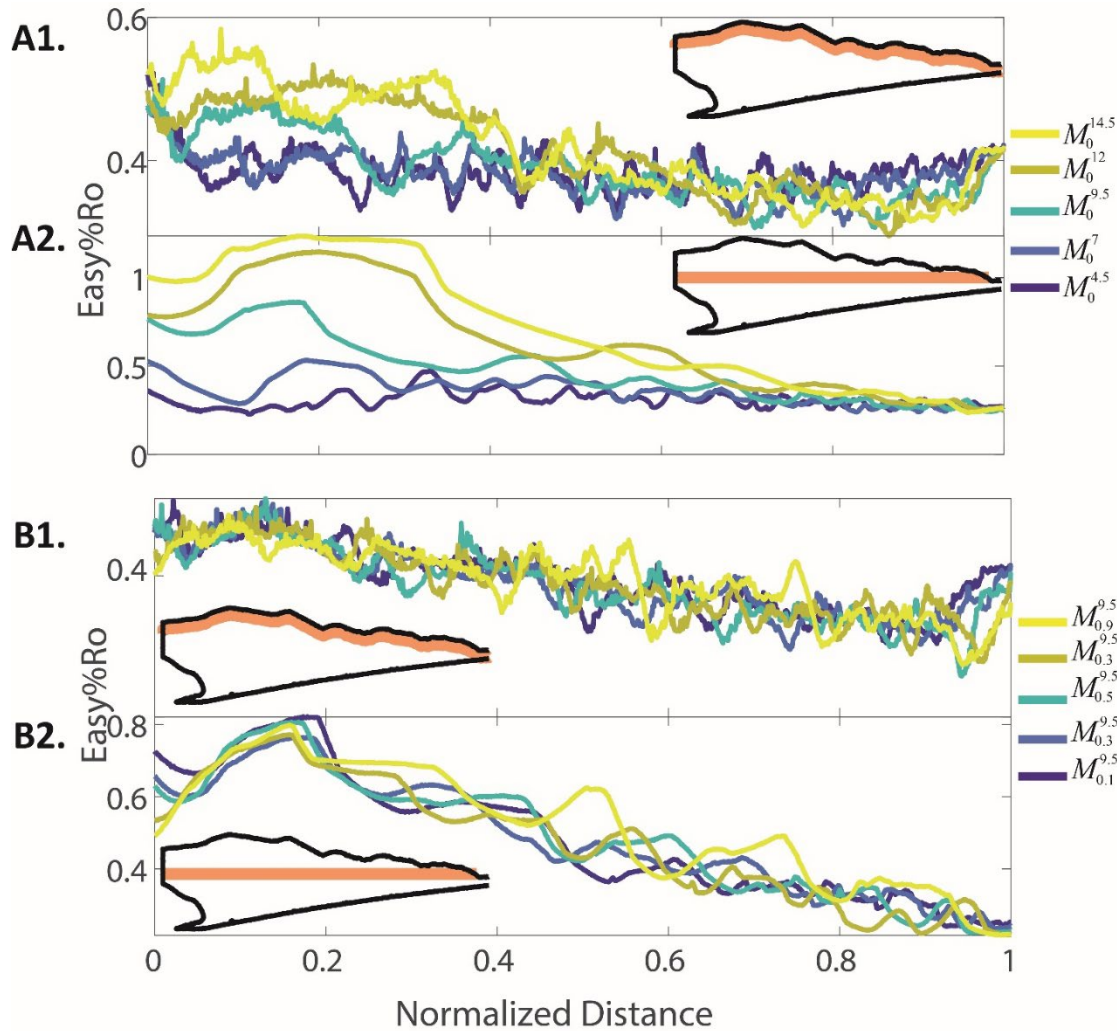
860 **Fig. 3:**  
 861 *Distribution of thermal maturity for different models at ~6.0 Myr (3.5 Myr of thermal maturation). Panels A1-A5 show the*  
 862 *thermal maturity distribution (computed using Easy%Ro) in subduction wedges of models as a function of décollement strength*  
 863 *, respectively. A6-A10 show the thermal maturity distribution in subduction wedges of models function of sedimentation rate ,*  
 864 *respectively. The grey color of the markers indicate that no thermal maturity change in these sediments have not occurred.*  
 865 *B1-B10 and C1-C10 similarly show the thermal maturity distribution in subduction wedges computed using Simple%Ro and*  
 866 *Basin%Ro, respectively.*

867



868 **Fig. 4:**

869 The variation of % $R_o$  for a horizon as indicated by the orange band in the inset at 7.5 Myr. Panel A1 and A2 shows all the  
870 models with different decollement strength. Panel B1 and B2 shows all the models with different sedimentation rates. Horizons  
871 in panel A1 and B1 are located at 1 km depth from the surface, whole in panel A2 and B2 the horizons are horizontal zones  
872 located at the trench depth. The horizontal distance from the backstop is normalized by the wedge length. Horizontal distance  
873 0 represents the fixed backstop and 1 represents the trench.  
874



875

876

877

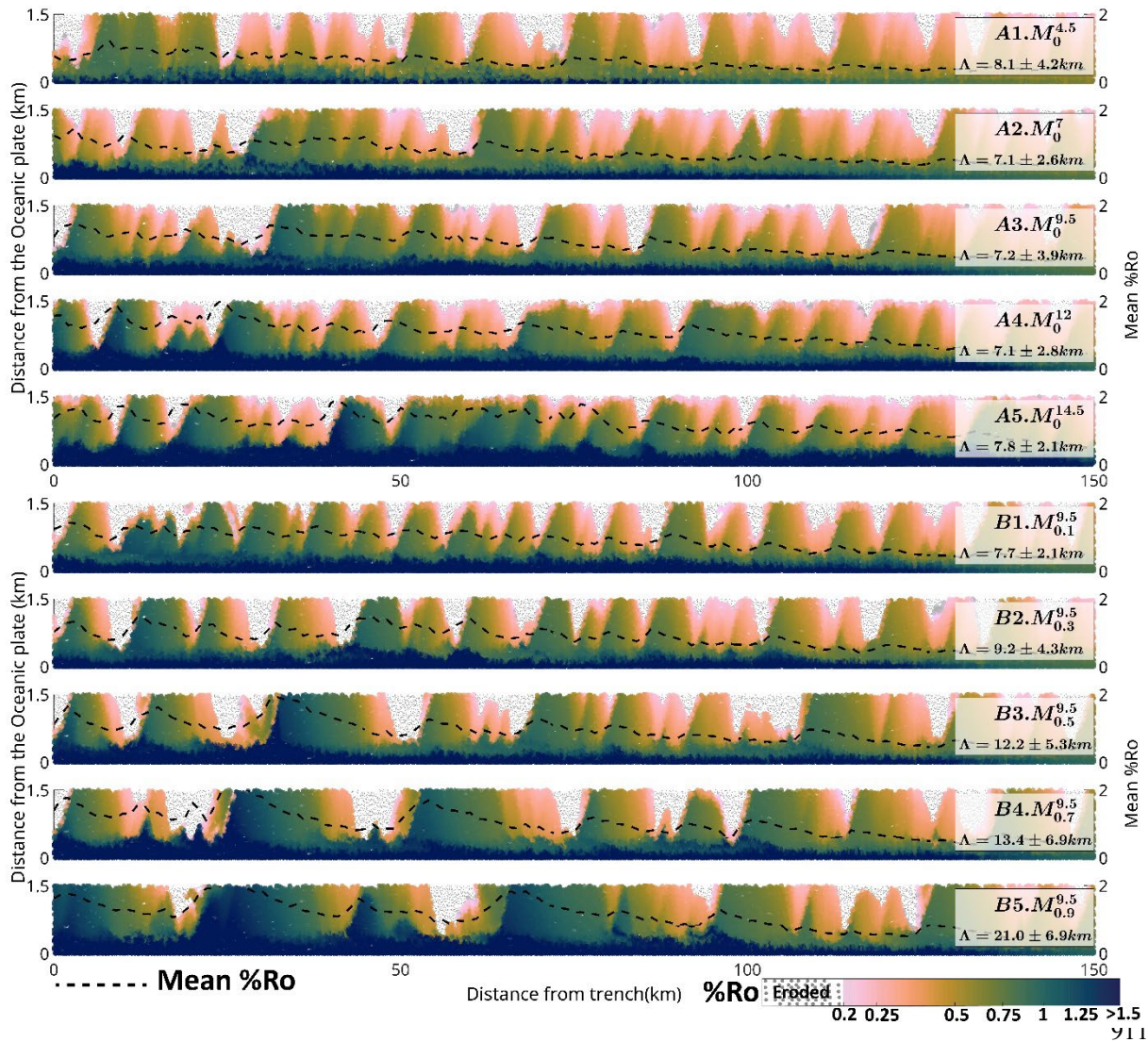
878

879

880  
881  
882  
883  
884  
885  
886

**Fig. 5:**

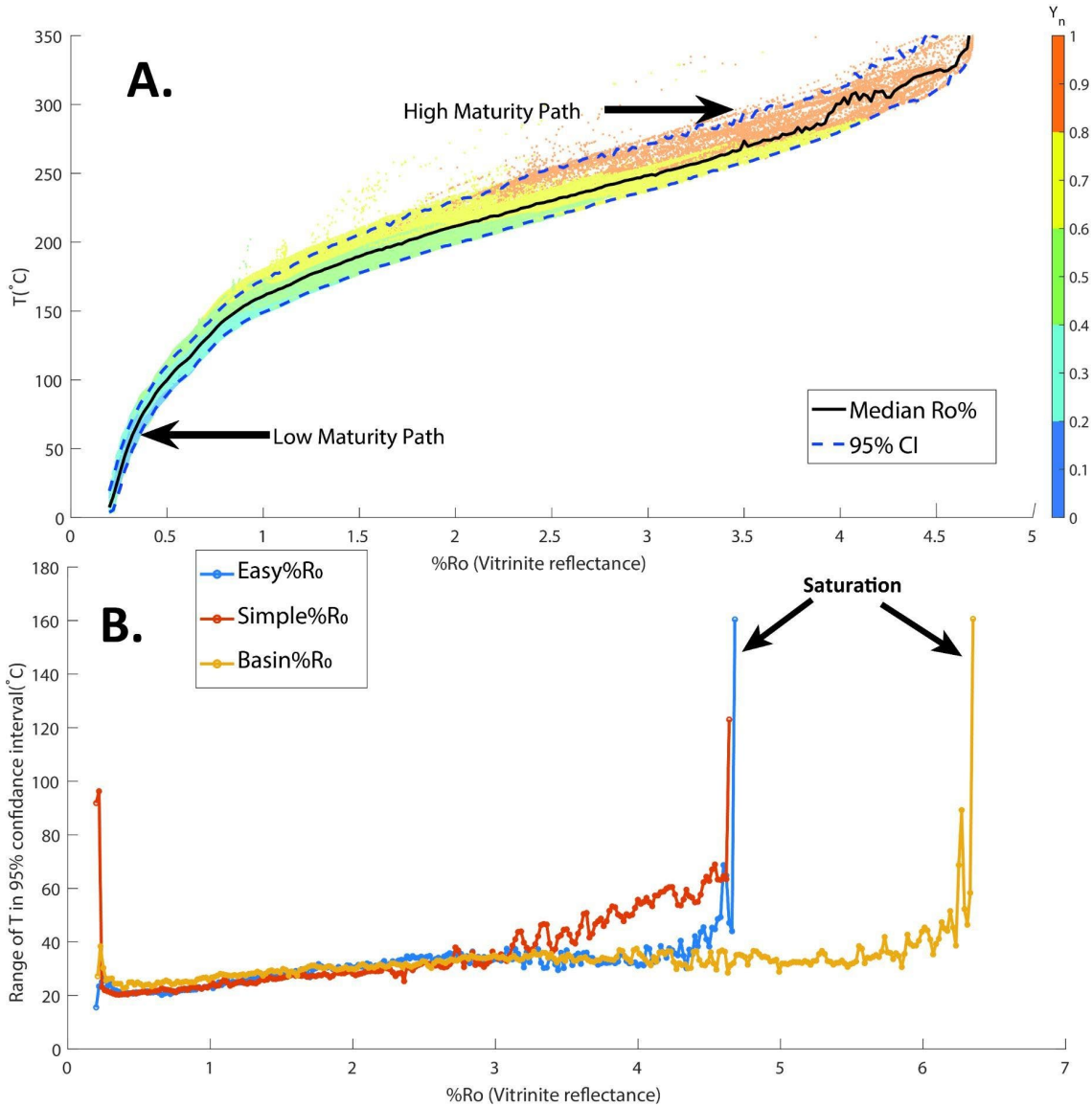
Map of thermal maturity at 7.5 Myr mapped to sediments at 2.5 Myr. Panel A1-A5, B1-B5 show the mapping for models - and - respectively. The vertical axis (distance from the oceanic plate) has been corrected for the bending of the plate. The horizontal axis represents the distance of sediments from the trench. The grey colour of the markers indicates that these sediments have been eroded/reworked due to slope failure. The broken black line represents the mean %Ro attained sediment at a given distance from the trench.  $\Lambda$  represents the horizontal periodicity in mean %Ro for the given model.



912  
913

914 **Fig. 6:**

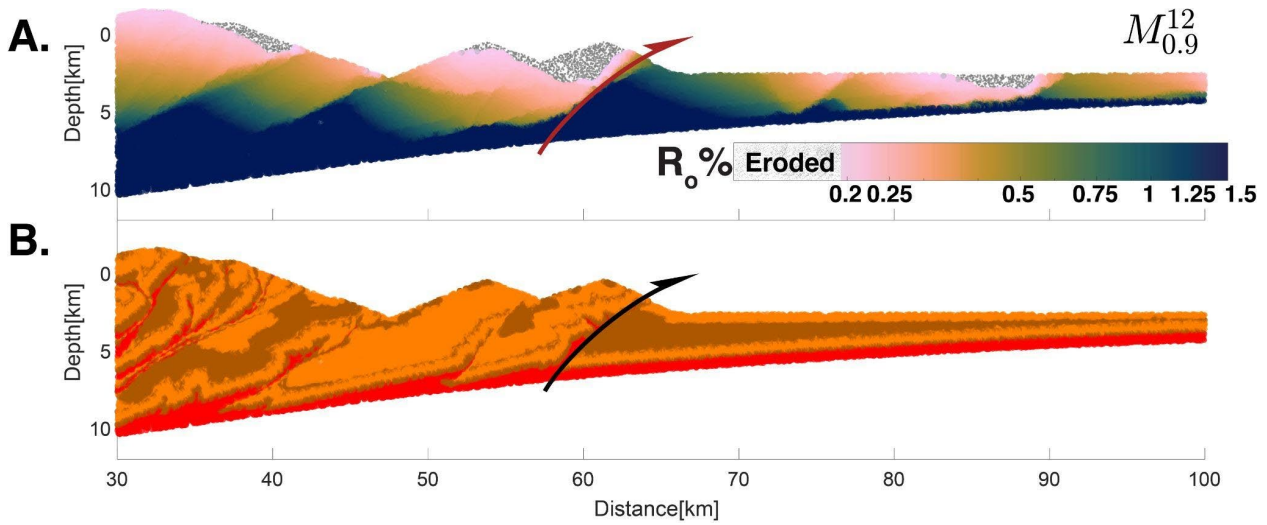
915 *A. Vitrinite Reflectance (%Ro) vs Maximum Exposure temperature in all models. The colours in panel A represent the depth*  
916 *of the sediments at 7.5 Myr normalized by the thickness of the wedge ( $Y_n$ ). B. Range of 95% CI for Easy%Ro, Simple%Ro and*  
917 *Basin%Ro.  $Y_n$  is the depth of the marker from the surface normalized by the thickness (vertical extent) of the wedge at the*  
918 *location of the marker. Please see panel B of Fig. S16 for computation of  $Y_n$*   
919



920

921 **Fig. 7:**

922 Mapping of eventual thermal maturity (vitrinite reflectance at 7.5Myr) to the location of same markers at ~4Myr in model .  
923 Panel A shows the values of thermal maturity for the markers while the lithology of the wedge is shown in panel B. The half  
924 arrow represents the active frontal thrust. The sediments which were eroded by 7.5Myr but exist at 4Myr have been markers  
925 eroded using dotted grey points.



926

927

928

929

930

931

932

933

934

935

936

937

938

939

940

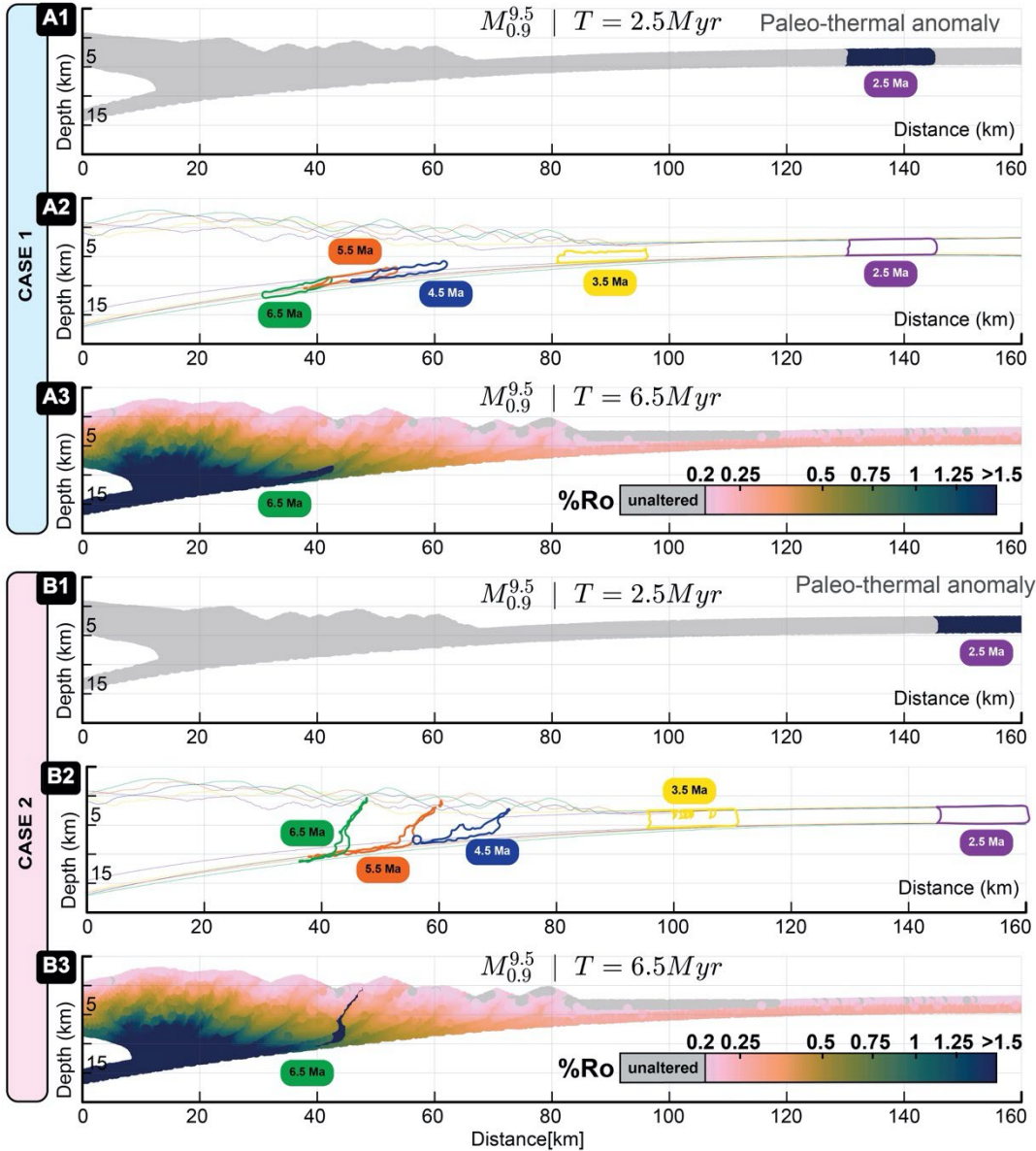
941



942  
943  
944  
945  
946  
947  
948  
949

**Fig. 8:**

Position dependency of thermal maturity preservation. A1. Distribution of %R<sub>0</sub> at 2.5 Myr with a paleo-thermal anomaly emplaced at 130-145 km from the backstop. A2. The evolution of the emplaced paleo-thermal anomaly from 2.5 Myr to 6.5 Myr in case 1. A3. Distribution of %R<sub>0</sub> at 2.5 Myr. B1. Distribution of %R<sub>0</sub> at 2.5 Myr with a paleo-thermal anomaly emplaced at 145-160 km from the backstop. B2. The evolution of the emplaced paleo-thermal anomaly from 2.5 Myr to 6.5 Myr in case 2. B3. Distribution of %R<sub>0</sub> at 2.5 Myr with a paleo-thermal anomaly emplaced at 145-160 km from the backstop.



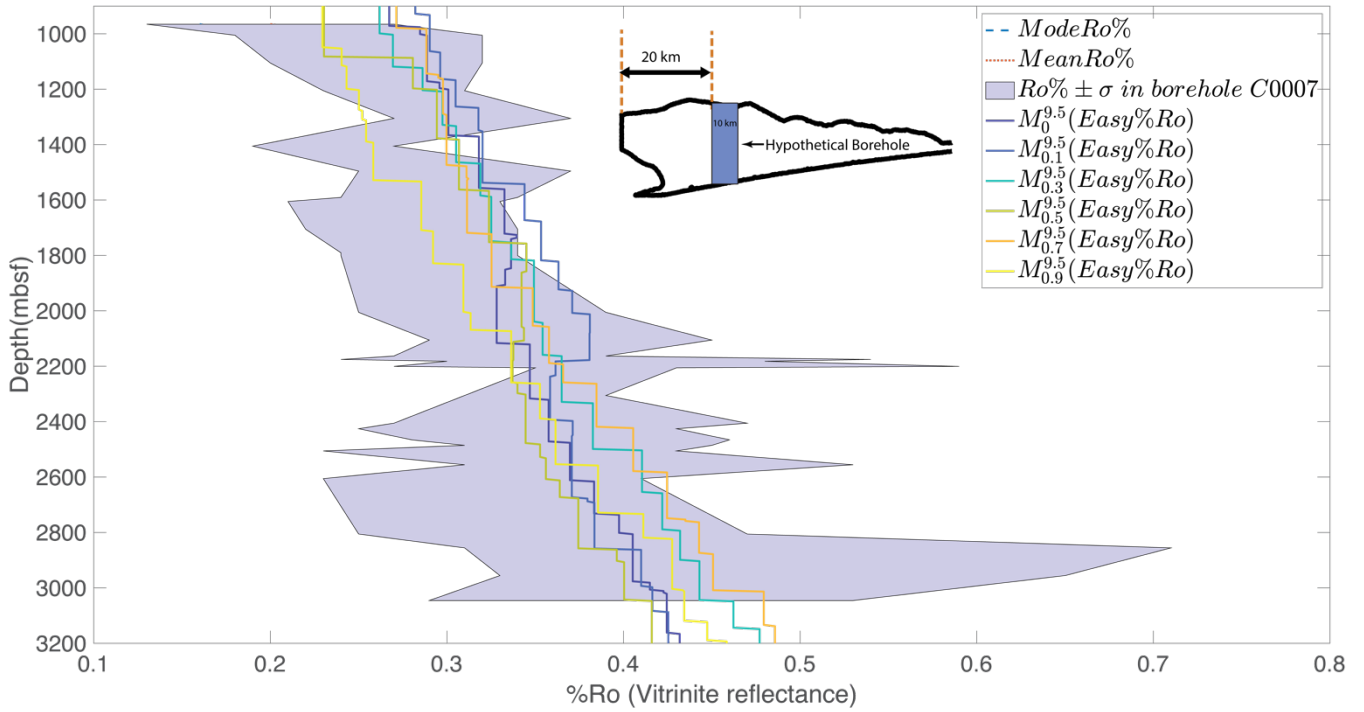
950  
951

952

953

954 **Fig. 9:**

955 *Depth vs Thermal maturity (%Ro). The shaded (in violet) region shows the range of observed Ro% (mean±1SD) from the C0002*  
956 *borehole ,colored lines represent the values in models sampled from a 10 km wide hypothetical borehole 20km seaward of the*  
957 *backstop as shown in the inset .*  
958



959

960

961

962